Mobility of carbon-decorated screw dislocations in bcc iron

Lisa Ventelon, Daniel Caillard, Bérengère Lüthi, Emmanuel Clouet, David Rodney, François Willaime

▶ **To cite this version:**

Lisa Ventelon, Daniel Caillard, Bérengère Lüthi, Emmanuel Clouet, David Rodney, et al.. Mobility of carbon-decorated screw dislocations in bcc iron. Acta Materialia, 2023, 247, pp.118716. 10.1016/j.actamat.2023.118716 . hal-04501043

HAL Id: hal-04501043
https://hal.science/hal-04501043v1

Submitted on 3 Jun 2024

HAL is a multi-disciplinary open access archive for the deposit and dissemination of scientific research documents, whether they are published or not. The documents may come from teaching and research institutions in France or abroad, or from public or private research centers.

L'archive ouverte pluridisciplinaire **HAL**, est destinée au dépôt et à la diffusion de documents scientifiques de niveau recherche, publiés ou non, émanant des établissements d'enseignement et de recherche français ou étrangers, des laboratoires publics ou privés.

Mobility of carbon-decorated screw dislocations in bcc iron

Lisa Ventelon[a,*], Daniel Caillard[b], Bérengère Lüthi[a], Emmanuel Clouet[a], David Rodney[c], François Willaime[d]

[a]*Université Paris-Saclay, CEA, Service de Recherches de Métallurgie Physique, 91191 Gif-sur-Yvette, France*
[b]*CEMES-CNRS, 29 rue Jeanne Marvig, BP94347, 31055 Toulouse, France*
[c]*Institut Lumière Matière, CNRS-Université Claude Bernard Lyon 1, F-69622 Villeurbanne, France*
[d]*Université Paris-Saclay, CEA, Direction Scientifique Énergies, 91191 Gif-sur-Yvette, France*

Abstract

We investigate the mobility of screw dislocations decorated by carbon solutes in body-centered cubic iron based on density functional theory (DFT) calculations and transmission electron microscopy (TEM) observations of in-situ straining experiments. We focus on the high-temperature domain, between 500 and 800 K, where plasticity is controlled by the slow glide of decorated screw dislocations with a mobility similar to the Peierls mechanism existing below 300 K, at variance with the athermal regime observed at intermediate temperatures. We propose that due to the strong pinning of reconstructed dislocation lines by carbon solutes, dislocation glide occurs by the formation and migration of kinks, both controlled by the jumps of carbon atoms. We calculate the associated kink-pair nucleation and formation energies as well as the migration energies of isolated kinks and use these DFT values to predict the dislocation velocity as a function of temperature, applied stress and dislocation length. The validity of the mobility law is assessed by the comparison with dislocation velocities measured in TEM observations at different temperatures and local shear stresses. The quantitative agreement between the experimental measurements and the analytical model supports the proposed glide mechanism and the DFT values obtained for kink energies.

Keywords: Plasticity, Dislocations, Iron, Carbon, Density functional theory, In-situ TEM straining experiments

1. Introduction

In-situ transmission electron microscopy (TEM) straining experiments [1, 2] carried out in iron containing a low carbon concentration, namely 3-4 wt. ppm of C, have shown that at high temperature, at the end of the so-called blue-brittleness regime near 500 K [3], and up to about 800 K, plasticity is unexpectedly controlled by the thermally-activated motion of straight screw dislocations. This behaviour suggests that in this high-temperature regime, dislocation glide proceeds through the nucleation and migration of kink-pairs along the dislocation lines, as below room temperature in pure Fe [4]. The reappearance of the Peierls mechanism at high temperature in Fe-C is proposed to result from the strong attraction of screw dislocations with carbon atoms, as evidenced by density functional theory (DFT) calculations in most body-centered cubic (bcc) transition metals, leading to their transformation and pinning in the hard core configuration with regular trigonal prisms of metal atoms centered on carbon atoms [5–10]. This segregation of solutes in the dislocation core leading to a core reconstruction was also evidenced using DFT with other interstitial solute elements [11–15] and is observed with embedded atom method (EAM) potentials [16].

At high temperatures, the carbon atoms can diffuse and segregate on screw dislocation cores. A thermodynamical model parameterized on DFT calculations showed that at equilibrium, half of the prismatic core sites are occupied by carbon atoms over a large temperature domain between 400 and 600 K [17]. The mobility of decorated screw dislocations has therefore to be investigated accounting for this segregation of carbon atoms in the dislocation core. This requires to determine the activation energies involved during the formation and migration of kink-pairs on a screw dislocation decorated by carbon atoms.

DFT calculations are used in the present work to obtain all ingredients necessary to model the dislocation velocity in the temperature range where carbon segregates on screw dislocations, i.e. the kink-pair forma-

*Corresponding authors
Email address: lisa.ventelon@cea.fr (Lisa Ventelon)

tion energy, the migration and nucleation energies. The resulting kinetic model parameterized on DFT calculations is then compared to experimental measurements. To this end, in-situ TEM straining experiments in Fe-C are performed at three different temperatures, corresponding to the end of the blue-brittleness regime, where the mobility of dislocations is controlled by the nucleation and propagation of kinks. Both the dislocation velocities and the local shear stress are measured experimentally allowing to test the validity of the theoretical mobility law. We also use these TEM observations to measure the critical kink-pair extension corresponding to the transition length between the length-dependent and kink-collision regimes. These delicate and detailed experimental measurements make it possible to quantitatively compare the velocity law predicted from ab initio with the experimental one.

2. Ab initio investigation

2.1. Methodology

We consider a quadrupolar periodic array of dislocation dipoles [18], with carbon atoms separated by $2b$ along the $\langle 111 \rangle$ direction of the dislocation line (b is the dislocation Burgers vector equal to $1/2\langle 111 \rangle$), as illustrated in Figs. 1(b) and (c). This carbon-carbon separation distance along the line corresponds to every other prismatic core site occupied by a carbon atom, as predicted by ab initio-based thermodynamics [17]. For completeness, we also consider a fully saturated dislocation line shown in Fig. 1(a) with all the prismatic sites occupied by carbon atoms, corresponding to a separation distance of $1b$ between carbon atoms along the line. The simulation cell contains 135 Fe atoms per length b of dislocation line, with periodicity vectors given in Ref. [19]. Cell sizes of $4b$ and $8b$ along the dislocation line, denoted h, are used with respectively $1 \times 2 \times 4$ and $1 \times 2 \times 2$ shifted k-point grids. This configuration results in 540 and 1080 Fe atoms in the simulation cell for resp. $h = 4b$ and $h = 8b$. Spin-polarized DFT calculations are performed with the Vasp code [20] using the projector augmented wave scheme [21, 22] and the Perdew–Burke–Ernzerhof generalized gradient approximation. Pseudopotentials without semicore electrons for Fe and with s and p valence electrons for C are used with a 400 eV kinetic-energy cutoff and a 0.2 eV Methfessel-Paxton electronic occupancy smearing. The atomic structures are determined by performing ionic relaxations in fixed cells using a criterion of 10 meVÅ^{-1} for force convergence.

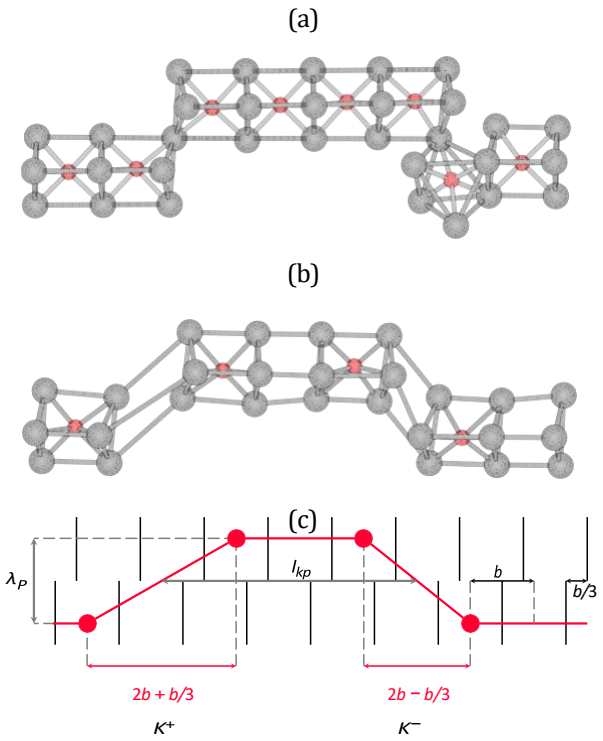

Figure 1: Atomic structure of a reconstructed screw dislocation with a kink-pair and carbon-carbon separations of (a) $1b$ and (b) $2b$. The $2b$ case is represented schematically in (c), highlighting the shift of $b/3$ between prismatic sites in successive Peierls valleys. In (a) and (b), the Fe atoms in contact with the dislocation core are shown in gray, the C atoms in red. The configurations are obtained after DFT relaxation in the $8b$-cell.

We consider kinks lying on {110} planes. Two nonequivalent kinks can form on a screw dislocation, sometimes erroneously called vacancy- and interstitial-type kinks [23–27]. Here, we adopt the notation proposed in Ref. [28] and use a + superscript (denoted K^+ for positive kink in Fig. 1) if the dislocation line in the kink is rotated towards the other $\langle 111 \rangle$ close-packed direction in the {110} plane (i.e. the direction forming an angle of 71° with b), and a − superscript (denoted K^- for negative kink in Fig. 1) in the opposite case. To calculate the kink-pair formation energy, a pair of kinks of opposite sign is introduced along both dislocations composing the dislocation dipole, unless otherwise specified. The kink separation, i.e. the separation distance between opposite kinks, denoted by w_{kp} thereafter, is set equal to half the cell size along the dislocation line, i.e. $2b$ in the $4b$-cell and $4b$ in the $8b$-cell. The kink height, denoted λ_P, is set to one Peierls valley, i.e. $\lambda_P = \sqrt{2}/3a_0$ with a_0, the lattice parameter (2.83 Å).

2.2. Kink-pair formation energy

Whether the kink separation is set to $2b$ or $4b$ and for both carbon distributions along the reconstructed lines (Figs. 1(a) and 1(b)), we find upon relaxation that both the negative and positive kinks are very abrupt with a width set by the distance between C atoms along the line, i.e. $1b$ to $2b$, in contrast with the case of pure iron, where the kinks along the easy core configuration are spread over $20b$ approximately [27, 29, 30]. All the carbon atoms remain in the prismatic core sites during energy minimization except for one particular configuration. In the case of the fully saturated dislocation line, as seen in Fig. 1(a), the carbon atom situated in the negative kink relaxes from its prismatic core site towards the nearest neighbouring octahedral site, for kink separations of both $2b$ and $4b$. Similar kink relaxation has been observed in W-C system [31]. This can be linked to the fact that the K^+ and K^- kinks have different atomic arrangements. As illustrated in Fig. 1, prismatic sites are shifted by $b/3$ in successive Peierls valleys. As a result, the K^+ kink has a width $2b/3$ longer than the K^- kink. The C-C distance in the K^- kink is thus compressed. During relaxation, due to the strong first-neighbour repulsion between C atoms, one C atom moves away from the core to an octahedral position, which corresponds to the fourth neighbour octahedral site of the reconstructed core for the forward dislocation segment. This position has been shown energetically stable for half-filled reconstructed cores of straight dislocations [17].

The reference configuration used in the calculation of the kink-pair formation energy is the straight dislocation in the hard core configuration with the carbon atoms in the prismatic core sites. The obtained kink-pair formation energy is 0.44 eV (resp. 0.28 eV) when the opposite kinks are separated by $2b$ and the C-C separation distance is $2b$ (resp. $1b$). Upon increasing the distance between the opposite kinks, the formation energy increases to 0.60 eV (resp. 0.50 eV) for a kink separation w_{kp} of $4b$ and a C-C separation distance of $2b$ (resp. $1b$). These uncorrected DFT values, denoted E_{DFT} correspond to the circles in Fig. 2. The increase of E_{DFT} with w_{kp} reflects the elastic interaction energy between the kinks, which varies as $1/w_{kp}$. Indeed, given the small separation distances between the kinks belonging to the same dislocation line, part of the obtained formation energy corresponds to the elastic interaction between opposite kinks composing the kink-pair as well as between these kinks and their periodic images. In the following, in order to estimate the corresponding elastic interaction energy, the kink-pair is regarded as being composed of straight orthogonal line segments (i.e. with no kink-width). Considering two opposite straight kinks

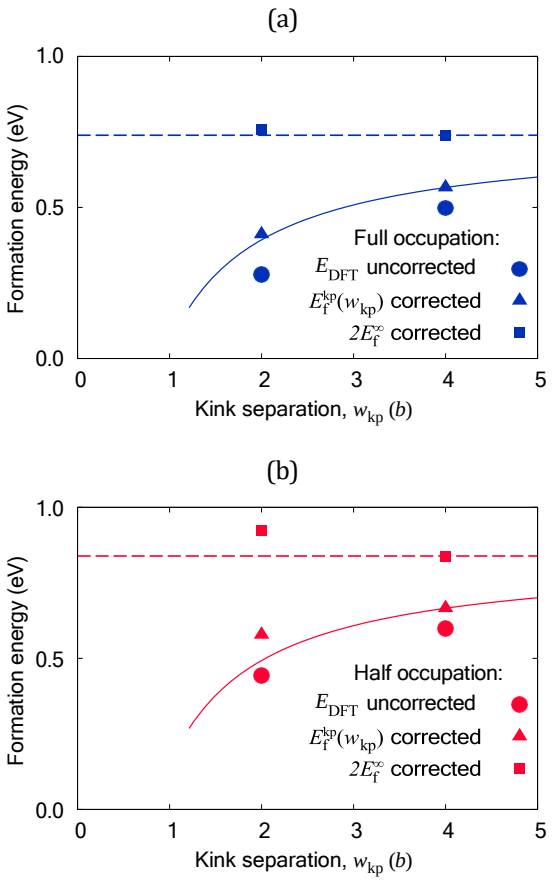

Figure 2: Uncorrected and corrected kink-pair formation energies as a function of the separation distance between both kinks in the case of (a) a full saturation of the prismatic core sites and (b) a half-occupation with every other prismatic site occupied by a carbon atom. The solid lines correspond to the analytic model of finite separation distance and the dashed lines correspond to the best estimate of the formation energy of a pair of isolated kinks. Note that these lines pass through the points for $w_{kp} = 4b$, i.e. corresponding to the case where the elastic correction is expected to work the best.

in an otherwise infinite straight dislocation and assuming that $w_{kp} \gg \lambda_P$, the interaction energy between kinks of opposite sign in the general anisotropic elastic case is [32]:

$$W_{int}(w_{kp}) = -\frac{1}{2}\left[E(\theta) + E^{II}(\theta)\right]\frac{\lambda_P^2}{w_{kp}}. \qquad (1)$$

θ is the dislocation orientation ($\theta = 0$ for a screw orientation) and $E(\theta)$ is the prelogarithmic energy factor of the elastic energy for an infinite straight isolated dislocation with the same Burgers vector b. This interaction energy is attractive provided that the line tension $E(\theta) + E^{II}(\theta) > 0$. Simple explicit solutions for $E(\theta)$ exist in isotropic media as a function of the Poisson

ratio and shear modulus. In an anisotropic elastic media, $E(\theta)$ can be numerically evaluated using the BaBeL code [33]. For the screw orientation, the line tension coefficient $\Gamma = \frac{1}{2}(E(0) + E^{II}(0))$ is 0.32 eVÅ^{-1} using 299, 153, and 103 GPa for the elastic constants C_{11}, C_{12}, and C_{44} resp. [34]. To obtain the formation energy of a pair of isolated kinks, the formation energy calculated with DFT (circles in Fig. 2) is corrected by subtracting the interaction energy arising from both the periodic boundary conditions (W_{int}^{PBC}) and the interaction between opposite kinks composing the kink-pair ($W_{int}^{supercell}$). Both interaction energy contributions are given by (see Appendix A):

$$W_{int}^{PBC} = -\Gamma \frac{\lambda^2}{w_{kp}} (2 \ln 2 - 1), \quad (2)$$

$$W_{int}^{supercell} = -\Gamma \frac{\lambda^2}{w_{kp}}. \quad (3)$$

Eqs. 2 and 3 are used in Fig. 2 to extract the formation energy of the kink-pair with finite kink separation w_{kp}, denoted $E_f^{kp}(w_{kp})$, and the formation energy of a pair of isolated kinks, i.e. with $w_{kp} \to \infty$, denoted $2E_f^{\infty}$:

$$E_f^{kp}(w_{kp}) = E_{DFT} - W_{int}^{PBC}, \quad (4)$$

$$2E_f^{\infty} = E_f^{kp}(w_{kp}) - W_{int}^{supercell}. \quad (5)$$

As seen in Fig. 2, whether the carbon atoms are separated by 1*b* or 2*b* along the dislocation line, the corrected formation energies for the isolated defect depend very weakly on the simulation cell size along *b*, which shows the validity of the elastic model. The best estimate for the formation energy of a pair of isolated kinks is 0.84 eV (resp. 0.74 eV) for C-C distances of 2*b* (resp. 1*b*) along the line. Its decrease with decreasing carbon-carbon separation distance along the dislocation line can be linked to the strongly repulsive nearest-neighbour C-C interaction along the line evidenced in a previous DFT study (+0.21 eV [5]). Indeed, in the case of carbon atoms separated by 1*b*, this strong repulsion is reduced with the presence of the kink-pair as the carbon atoms are moved appart from, while in the case of C-C distance of 2*b*, this effect is weaker as the carbon atoms are already far away from one another in the straight dislocation.

Note that the configuration, where the kink-pair is introduced only on one of the two dislocation lines composing the dislocation dipole, the other dislocation remaining straight, was also investigated in the case of carbon-carbon separation distance of 2*b* and kink separation of 2*b*. The resulting uncorrected kink-pair formation energy varies by less than 10 meV compared to the configuration where both dislocation lines contain a kink-pair. This justifies our choice to neglect the elastic interaction between kinks belonging to different dislocation lines in the elastic correction.

2.3. Kink migration energy

In order to compute the migration energies of isolated kinks, one positive (resp. negative) kink was introduced in a cell containing 585 (resp. 495) Fe atoms along each straight screw dislocation composing the dipole, following the methodology in Ref. [27]. The kink migration energy was calculated using the Nudged Elastic Band (NEB) method by displacing one of the two kinks in the 4*b*-cell by a distance of 2*b* (resp. 1*b*) along the dislocation line in the case of a C-C separation distance of 2*b* (resp. 1*b*), with seven intermediate NEB images in both cases. As illustrated in Fig. 3(a), this process involves the migration of a carbon atom between successive Peierls valleys. The kink on the second dislocation is kept immobile in order to avoid a non-simultaneous migration of the two kinks along the NEB path.

The DFT calculations show that kinks go through a non-negligible energy barrier when propagating along the dislocation line (Fig. 3(b)), contrary to pure iron where kinks are highly mobile [27]. We note that the initial and final states for both carbon distributions have the same energy, justifying again neglecting the elastic interaction between kinks belonging to different dislocation lines. Thus no elastic correction is applied in this set of calculations. The migration barriers calculated for both kinks evidence an easier migration for the positive kink compared to the negative kink, both for a full (0.58 eV vs 1.52 eV) or a half occupation of the prismatic sites (0.90 eV vs 1.01 eV). This asymmetry results from the asymmetry between the K^+ and K^- kinks illustrated in Fig. 1. The carbon-carbon distance varies along the migration path and notably, at the saddle point, the distance between carbon atoms in the K^- kink is shorter than in the K^+ kink (for a half occupation of the prismatic sites, 4.7 and 5.5 Å resp.). Thus at the saddle point, the carbon atom has less space during the migration of the K^- kink than during the migration of the K^+ kink, resulting in a higher migration barrier for the K^- kink. This asymmetry is more pronounced in the case of a fully saturated dislocation line as the carbon atoms are closer to one another. The migration barrier is highest in the case of the negative kink on a fully saturated line as in this particular configuration, the kink migration involves the displacement of two carbon atoms:

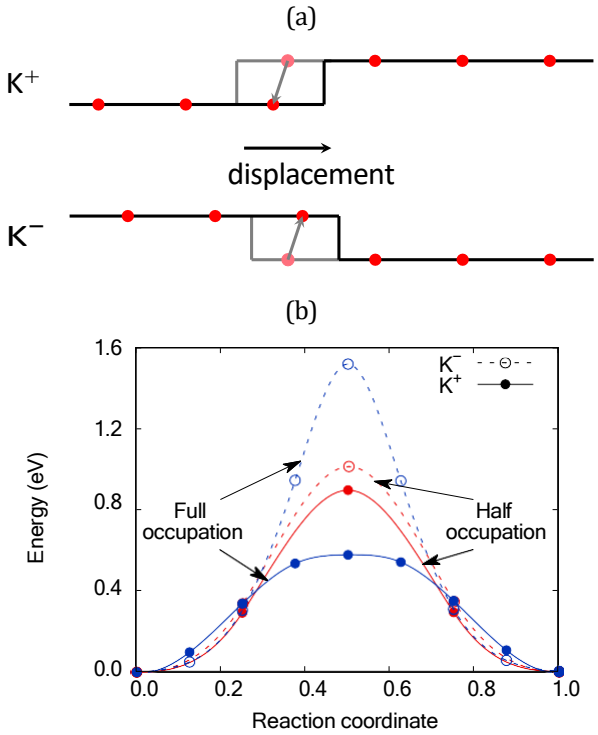

Figure 3: (a) Schematic representation of the migration of the positive and negative kinks. A dislocation segment of 1*b* or 2*b* (depending on the carbon-carbon separation distance along **b**) is displaced to the neighbouring Peierls valley following the motion of a carbon atom. The dislocation lines are represented in gray (before kink migration) and black (after migration) and the carbon atoms in light red (before kink migration) and red (after migration). (b) Energy variation during the migration of the positive and negative kinks in the case of carbon-carbon distances of 1*b* (in blue) and 2*b* (in red) along the dislocation line. The distance between two kinks along the dislocation line is 4*b*.

the carbon atom situated in the negative kink initially occupies an octahedral site (Fig. 1(a)) and jumps during the kink migration into a prismatic site while a neighbouring carbon atom in a prismatic site moves towards an octahedral site. The other kink migrations – the positive kink migration and the kink migrations for a half occupation of the prismatic sites – involve the jump of one carbon atom between prismatic sites.

The migration energies obtained for a half occupation of the prismatic sites are close to the migration energy of carbon in bulk Fe (0.86 eV in the present work in agreement with other DFT studies [35, 36] and the experimental value, namely 0.87 eV [37]). This shows that carbon atom migration controls the kink migration in Fe-C in this high temperature regime. The presence of the secondary Peierls valleys contrasts with the case of pure Fe, where kinks can migrate freely along the line [27].

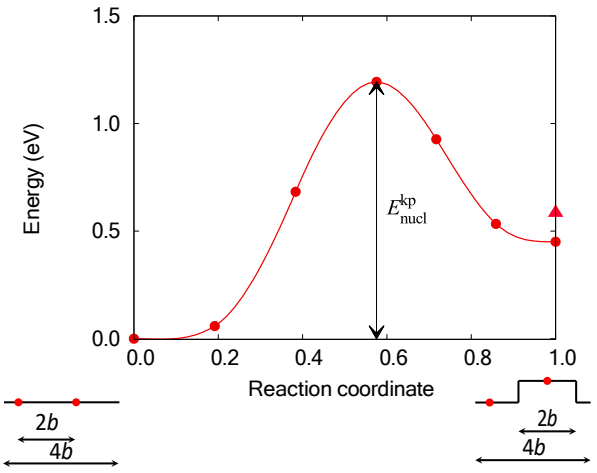

Figure 4: Energy variation for kink-pair nucleation in the case of carbon-carbon distance of 2*b* along the dislocation line. The kink separation is equal to 2*b* and the distance between a single kink and its image along the line is equal to 4*b*. The triangle symbol represents the corrected DFT formation energy of the kink-pair, where interactions with periodic images along the line are subtracted.

2.4. Kink-pair nucleation energy

The energy barrier for the nucleation of a kink-pair is calculated using the NEB method in the case of a C-C separation distance of 2*b* in the 4*b*-cell with a kink separation of 2*b*. The initial state consists of two straight dislocation lines and the final state, of one straight line and the other line containing a kink-pair. The obtained nucleation energy for the kink-pair is 1.19 eV (Fig. 4). Note that in this calculation, the elastic correction arising from the interactions of the kinks with their periodic images is highest in the final state. The value of the corrected DFT formation energy of the kink-pair with finite kink separation, $E^{kp}_{f}(2b)$ is represented in Fig. 4 in the final state by a triangle, and compared to the uncorrected DFT energy of the final state in this NEB calculation. This shows that there is an error due to periodic boundary conditions of 0.16 eV at most in the energy barrier calculation for kink-pair nucleation.

3. Dislocation velocity law

Based on the above DFT results, summarized in Table 1, we use the model of Hirth and Lothe for the motion of dislocations in a material with high secondary Peierls barriers [38–40] to map in Fig. 5 the corresponding energy profile for kink diffusion as a function of kink separation. This results from the formation energy of the kink-pair, which varies with $1/w_{kp}$, on which the migration barrier for kink diffusion is superimposed (taken as the lowest migration barrier, i.e.

Table 1: Summary of the present DFT data (in eV) for separation distances of 1*b* and 2*b* between carbon atoms along the line.

	$E^{kp}_f(2b)$	$E^{kp}_f(4b)$	$2E^{\infty}_f$	E^{K+}_{mig}	E^{K-}_{mig}	E^{kp}_{nucl}
1*b*	0.41	0.57	0.74	0.58	1.52	-
2*b*	0.58	0.67	0.84	0.90	1.01	1.19

for the positive kink). Accounting for the half occupation of the core sites by carbon atoms, the spacing between bumps is 2*b* and the resulting activation energy is equal to the sum of the formation energy of a kink-pair and the migration energy of a positive kink, i.e. $2E^{\infty}_f + E^{K^+}_{mig} = 1.74$ eV for a pair of non-interacting kinks with an infinite separation distance. The nucleation energy barrier of a fresh kink-pair on a dislocation segment of length 4*b* (Fig. 4) corresponds to the first barrier in Fig. 5. The nucleation energy (1.19 eV) is therefore smaller than the activation energy for kink formation and migration (1.74 eV). Therefore the energy barrier controlling the motion of dislocations in Fe-C is not the nucleation energy barrier of the first kink-pair. The effect of an applied stress τ_a is also illustrated in Fig. 5 by adding a contribution $-\tau_a b \lambda_P w_{kp}$ corresponding to the work of the Peach-Koehler forces to the formation energy of the kink-pair.

The dislocation velocity can be expressed analytically as the product of the nucleation rate J_{kp} with the average kink-pair extension L_{kp}, i.e. the average kink-pair mean free path [39] [38, 39]. Using the classical nucleation theory, the nucleation rate can be written [31]:

$$J_{kp}(\tau_a, T) = \nu^- Z(\tau_a, T) \exp\left(-\frac{H^*_{kp}(\tau_a)}{kT}\right) \left[\exp\left(-\frac{E^{K+}_{mig}}{kT}\right) + \exp\left(\frac{E^{K-}_{mig}}{kT}\right)\right]. \quad (6)$$

In this expression, $H^*_{kp}(\tau_a)$ is the critical kink-pair nucleation barrier defined at the critical kink-pair size n^*, corresponding to a maximum of the kink-pair formation enthalpy, and $Z(\tau_a, T)$ is the Zeldovitch factor, which accounts for the fluctuations around the critical kink-pair size. The attempt frequency ν^- is considered as an adjustable parameter. In the following, we assume that the kink-pair formation energy follows the elastic interaction model given in Eqs. 3 and 5, and we consider a half occupation of the prismatic sites leading to a kink separation distance $w_{kp} = 2n\,b$, with n an integer. The kink-pair formation enthalpy can then be expressed as a function of the applied shear stress τ_a, and the kink separation $2n\,b$:

$$H_{kp}(n, \tau_a) = 2E^{\infty}_f - \frac{\Gamma \lambda_P^2}{2n\,b} - 2n\,\tau_a \lambda_P b^2, \quad (7)$$

where the contribution of an external stress τ_a is included (last term of Eq. 7). This results in:

$$n^*(\tau_a) = \frac{1}{2}\sqrt{\frac{\Gamma \lambda_P}{\tau_a b^3}}, \quad (8)$$

and

$$H^*_{kp}(\tau_a) = 2E^{\infty}_f - 2\sqrt{\Gamma \lambda_P^3 b \tau_a}. \quad (9)$$

Using the expression for the Zeldovitch factor $Z(\tau_a, T) = \sqrt{-\frac{1}{2\pi kT}\frac{\partial^2 H_{kp}}{\partial n^2}}_{n=n^*}$ [31], we obtain:

$$Z(\tau_a, T) = \frac{1}{\sqrt{\pi kT}} \sqrt[4]{\frac{\tau_a^3 \lambda_P b^7}{\Gamma}}. \quad (10)$$

Finally the dislocation velocity is given by [38, 39]:

$$v_d(\tau_a, T) = J_{kp}(\tau_a, T)\,\lambda_P \frac{L_{kp}(\tau_a, T)}{2b}. \quad (11)$$

Depending on the dislocation length L_d, two different expressions can be obtained for the average kink-pair extension L_{kp}, corresponding to a length-dependent regime and a kink-collision regime for the dislocation velocity [39]. The former regime prevails for short dislocation segments or low kink densities, where the kink-pair extension L_{kp} is equal to the dislocation length L_d.

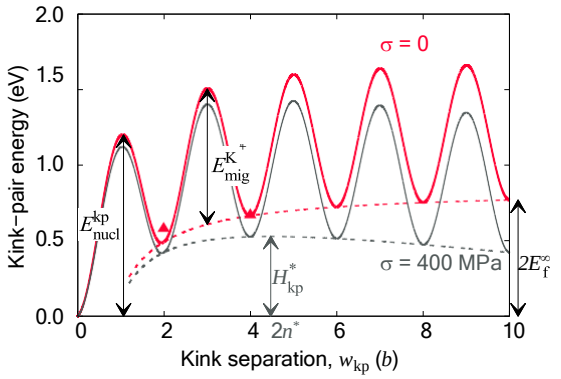

Figure 5: Energy profile for the nucleation and migration of a kink-pair as a function of kink separation without (red line) and with (gray line) an applied stress. In this model, every other prismatic site is occupied by a carbon atom. The triangles refer to the DFT data for the kink-pair formation energy after subtracting the interaction energy arising from the elastic interaction between a kink-pair and its periodic images along the line. The dashed lines refer to the analytic model of finite separation distance varying in $1/w_{kp}$.

The latter regime prevails for long segments or large kink densities, where the kink-pair extension is equal to the average distance $L_k^*{}_p$ travelled by both kinks between two collisions, given by:

$$L_k^*{}_p(\tau_a, T) = 2b\sqrt{\frac{v_k(\tau_a, T)}{J_{kp}(\tau_a, T)}}, \quad (12)$$

with v_k the kink velocity given by:

$$v_k(\tau_a, T) = 2b\nu^- \sinh\left(\frac{\tau_a \lambda_P b^2}{kT}\right) \left[\exp\left(-\frac{E^{K+}_{mig}}{kT}\right) + \exp\left(-\frac{E^{K-}_{mig}}{kT}\right)\right], \quad (13)$$

following the derivation explained in Ref. [31][1].

Transition between the length-dependent and the kink-collision regimes occurs when the dislocation length L_d becomes larger than $L_k^*{}_p$. Interestingly, Eq. 12 shows that this transition length does not depend on kinetic parameters like the attempt frequency ν^- or the kink migration energies, E^{K+}_{mig} and E^{K-}_{mig}, but only on the kink-pair formation energy. A smooth transition between both regimes can be described by considering the geometric average between both expressions of the kink-pair extension [31, 40], but such an average procedure is purely phenomenological. We will thus simply consider that the kink-pair extension is given by the minimum between the dislocation length and the critical kink-pair extension, $L_{kp}(\tau_a, T) = \min[L_d, L_k^*{}_p(\tau_a, T)]$.

Using Eqs. 6 and 10, all parameters appearing in Eq. 11 are known from the crystallography of bcc Fe and the DFT calculations presented in Section 2, except the attempt frequency ν^-, which is the only adjustable parameter. We will now test the validity of this velocity model by comparison with TEM in-situ straining experiments.

4. In-situ straining experiments

Previous experiments [1, 2] have shown the locking by C atoms of screw dislocations in iron above 500 K, with the reappearance of a Peierls regime for dislocation glide. In order to assess the validity of the mobility law deduced from our ab initio calculations, we performed TEM in-situ straining experiments in Fe-C at three temperatures, 523, 573 and 623 K and measured the dislocation velocities, as well as the local value of the applied shear stress. We also use these TEM observations to estimate the critical kink-pair extension L^*_{kp}, which marks the transition between the length-dependent and kink-collision regimes. A similar comparison was recently performed in bcc tungsten in presence of carbon [31]. But the comparison in W-C could not be as detailed as in Fe-C, because applied stresses were not measured experimentally. With this information extracted from experiments in Fe-C, a quantitative comparison becomes possible between experimental and theoretical velocities.

4.1. Experimental procedure

4.1.1. In-situ experiments

In-situ straining experiments were carried out in a JEOL 2010HC transmission electron microscope, at an accelerating voltage of 200 kV, and using a high-temperature straining holder designed in CEMES institute. The temperature is calibrated by observing the melting of several metallic samples in real operating conditions. Dynamic sequences were recorded by a Megaview III video camera working at 25 images per second, and analyzed frame by frame. Microsamples are rectangles with an electro-polished thin-edged hole, glued with a high-temperature cement on two rings adapted to the straining holder. Experiments were carried out in electrolytically pure iron containing 3 to 4 wt. ppm of C, less than 2 wt. ppm each of S, N, and Cr, and less than 5 wt. ppm each of O and P, provided by the École des Mines of St Étienne (France). Parts of these experiments have already been reported in Refs. [1, 2]. We discuss the measurement of the local stress before addressing the critical kink-pair extension.

4.1.2. Local stress measurement

The stress measurement is based on the observation of expanding and shrinking screw dipoles. This method is frequently used in materials where screw dislocations are subjected to high Peierls friction forces. It has been fully described in Refs. [4] and [41], in the case of pure iron strained at low temperature. As shown in Fig. 6(a), a screw dipole can expand when the work done by the local stress on the curved mixed dislocations closing the screw dipole is equal to or larger than the energy of the growing dipole, namely when the local shear stress τ_a is equal to or larger than the line tension stress $\tau_l(d)$

[1] Note that the factor of 2 appearing in the final expressions of the Zeldovitch factor (Eq. 10), the critical kink-pair size (Eq. 8) and the kink velocity (Eq. 13) compared to the expressions given in Ref. [31] comes from the fact that in the present work, kinks are gliding over a distance $2b$ for each migration event as only half of the core sites are occupied by C atoms, while kinks glide distance is $1b$ in tungsten where the dislocation core can be fully saturated by carbon atoms [10].

of the dipole. Both stresses are equal when the dipole width d (hereafter called critical width) is just sufficient to allow for dipole expansion. An approximate value of the dipole line-tension stress is $0.5\,\mu b/d$, with μ the shear modulus, which yields τ_l inversely proportional to d. More precise values deduced from anisotropic elasticity are used in the present case (see Ref. [4]).

In the same material strained at high temperature, there is however an additional friction stress τ_f necessary to trail the high density of carbon atoms segregated on the mixed dislocation core, as illustrated in Fig. 6(b). This friction stress is an average of the various friction stresses on the different characters of the curved dislocation. Then, the measurement of the line tension stress yields $\tau_l(d) = \tau_a - \tau_f$.

In order to estimate τ_f and τ_a separately, it is necessary to find narrower dipoles of width d', which shrink under the same conditions. As illustrated in Fig. 6(c), we have then $\tau_l(d') \geq \tau_a + \tau_f$. The inequality can be transformed in a strict equality if the shrinking dipole width d' can be considered as critical. Combined with the observation of an expanding dipole, we can thus obtain an upper value for the friction stress, $\tau_f \leq (\tau_l(d') - \tau_l(d))/2$ and then an upper value for the applied stress, $\tau_a \leq (\tau_l(d') + \tau_l(d))/2$. These values can be used as rough estimates of τ_f and τ_a. This procedure has been used in Ref. [42]. Note however that shrinking dipoles, which form by cross-slip, are rather rare and not observed in all experiments. Corrections taking into account dislocation movements in different slip planes with different Schmid factors are also necessary.

All these measurements allow us to determine τ_a in a given area of the microsample. However, the applied shear stress τ_a strongly varies with the observed area and local sample thickness. Stress and velocity measurements must accordingly be carried out in a same thick area of the microsamples.

4.1.3. Determination of the critical kink-pair extension

The length-dependent regime corresponds to short dislocation lengths $L_d < L_k^*{}_p$, where kinks can reach the dislocation extremities before another kink-pair is nucleated (Fig. 7(a)). Since the probability to nucleate kink-pairs is proportional to the dislocation length, the dislocation velocity is then also proportional to the length. The transition regime corresponds to $L_d \approx L_k^*{}_p$, where the probability to find two kink-pairs on the same dislocation is no longer negligible (Fig. 7(b)). The average kink-pair mean free path $L_k^*{}_p$ is then equivalent to the dislocation length L_d. The screw dislocation remains straight if the kinks of opposite signs can annihilate, namely if the two kink-pairs have been nucleated

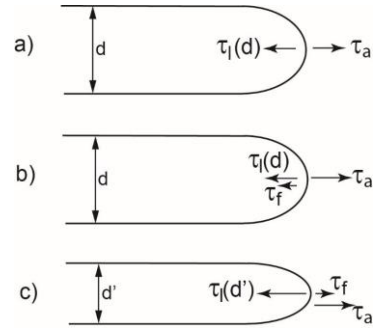

Figure 6: Illustration of the dislocation configurations used to measure the local shear stress τ_a and the friction stress τ_f. a) Expansion of a screw dipole in a pure material with no friction stress, for instance in pure iron at low temperature. b) Dipole expansion with friction stress τ_f (present case). c) Shrinking of a narrower dipole with the same friction stress.

in the same plane (case of strictly planar slip). However, in case of frequent cross-slip (wavy slip), kinks in different planes cannot annihilate, and a cross-kink is formed. This cross-kink pins the dislocation and eventually glides side-way and disappears at a dislocation extremity. Frequent observations of jogs or macro-jogs (jogs of several atomic distances height) on straight screw dislocations are thus characteristic of the transition. Since the transition is expected to be progressive at increasing dislocation lengths, the first observed macro-jogs are expected to correspond to the lower bound of the transition, and $L_k^*{}_p$ is considered to be slightly larger than the measured distances between macro-jogs.

The kink-collision regime corresponds to large dislocation lengths, $L_d > L_k^*{}_p$, where screw dislocations evolve towards the situation described in Fig. 7(c), because kinks accumulate at both dislocation extremities and tend to bend the dislocation. A steady state is reached for a central screw part of length $L_k^*{}_p$, because a new kink-pair is nucleated on average each time the length of this central part increases above $L_k^*{}_p$. Anchoring at jogs and macro-jogs can still be observed along the screw part.

Several methods can be thus used to estimate $L_k^*{}_p$:

1. Measurement of the screw dislocation velocity as a function of its length L_d, and observation of a departure from linearity at a length slightly lower than $L_k^*{}_p$, taking into account a progressive transition between the two regimes,
2. Observation of rectilinear screw dislocations anchored at one or several macro-jogs. $L_k^*{}_p$ is considered to be of the order of, or slightly larger, than the segment length between macro-jogs,
3. Observation of curved dislocations with a straight

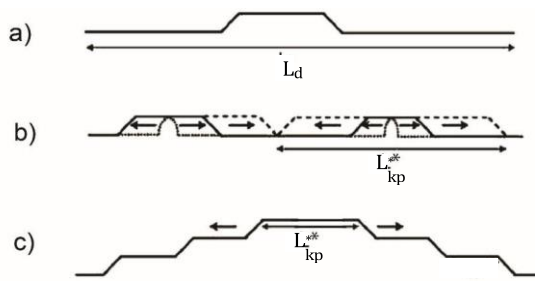

Figure 7: Schematic representation of the nucleation of kink-pairs on screw segments at increasing dislocation length. a) length-dependent regime, b) transition regime with kink collisions, c) steady state in the kink-collision regime.

screw part of more or less constant length equal to L^*_{kp}.

In all cases, it is necessary to prove that kinks are nucleated along the dislocation line, not at a surface. This is the case for instance when surface nucleation of kinks is not favored by line tension effects, i.e. when the screw direction is perpendicular to the intersection of the slip plane with the foil surface. Also, small curvatures of screw dislocations near the surfaces ensure that kinks are not nucleated at the surfaces.

4.2. Dislocation velocity and local stress

4.2.1. Experiments at 523 K

Fig. 8 shows an example of stress measurement. A screw dislocation noted s1 is anchored at a macro-jog and forms a loop in Fig. 8(a). The curved non-screw part glides to the bottom, emerges at the lower surface and forms a dipole of critical width d in Fig. 8(b). After appropriate geometrical correction, this width d gives the line tension stress $\tau_l(d)$. The remaining dipole of width d' in Fig. 8(c) subsequently disappears at the surface in Fig. 8(d). Having both an expanding and a shrinking dipole, we can estimate the applied shear stress and the friction stress, as explained in Section 4.1.2. After further geometrical corrections, we find that the applied shear stress is close to, or slightly below 140 MPa, and the friction stress is close to, or slightly below 40 MPa. This result and others are gathered in Table 2. In agreement with the discussion of the method presented in Section 4.1.2, the local stress strongly increases at decreasing sample thickness, which illustrates the necessity of carrying all measurements (stress and dislocation velocity or kink-pair mean-free path) in the same small area where the stress can be assumed uniform.

A few seconds later, another screw dislocation glides in the same area (Fig. 9, where A is the same fixed point as in Fig. 8). This dislocation is divided into two parts

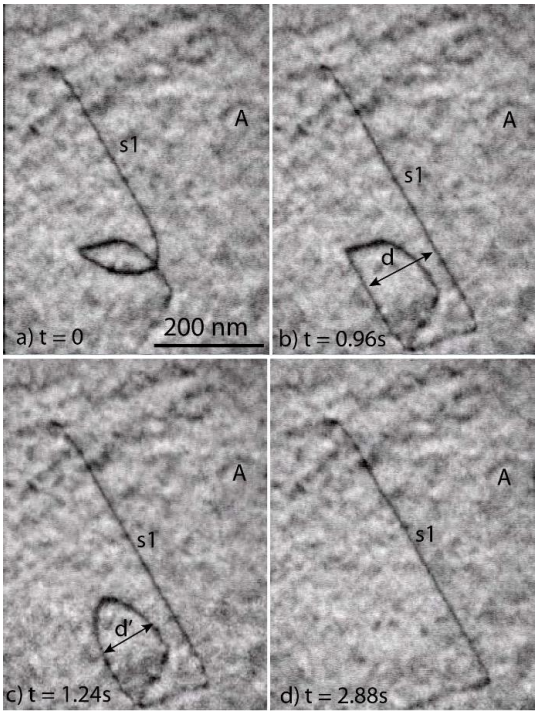

Figure 8: Local shear stress measurement at 523 K on a screw dislocation s1 moving to the right. (a) and (b) Expansion of a dipole of width d. (c) and (d) Shrinking of a dipole of width d'. A is a fixed point. See corresponding video as Supplementary material.

after its anchoring at a cross-kink forming a macro-jog in Fig. 9(a). The upper part s2 moves to the right and leaves a slip trace at the upper foil surface. It simultaneously increases its length until reaching a maximum length in Figs. 9(c) and 9(d). Then, a second macro-jog (noted MJ) is formed and the length of s2 decreases accordingly in Fig. 9(e). It is important to note that the slip trace is perpendicular to the screw direction, and that the screw dislocation is slightly bent at the surfaces, which ensures that kinks are not nucleated at the surfaces. It is thus possible to measure the velocity of s2 as a function of the length of its rectilinear (pure screw) part, in a case without surface kink nucleation. We estimate at ~50 nm the uncertainty on the dislocation length measurement associated with the difficulty to discriminate the dislocation rectilinear screw portion from its mixed bent extremities.

Velocities measured for this dislocation s2 are shown with red squares in Fig. 10. Experimental data points display a clear proportionality between the dislocation velocity and its length[2], in agreement with the length-dependent regime of the kink-pair glide mech-

[2]A shift of 50 nm is applied to the rough measurement of dislo-

Table 2: Local shear stress values as a function of sample thickness and corresponding estimates of the kink-pair mean free path $L_k{}^*_p$ deduced from TEM in-situ straining experiments. The values used in Fig. 13 are in italic, and the most reliable and complete set of values is in bold. The stress values are given ±25 MPa in average.

T (K)	$\tau_l(d)$ (MPa)	$\tau_l(d')$ (MPa)	τ_f (MPa)	τ_a (MPa)	Thickness (nm)	$L_k{}^*_p$ (nm)
523	192	250	≈ 80	≈ 270	300	
	107	135	≈ 40	≈ 150	425	
	103	***128***	≈ ***40***	≈ ***140***	***450***	***600 ± 100***
	128	174	≈ 60	≈ 186	400	
	114	127	> 35 [a]	> 149	400	
573	250				226	
	210				190	
	110				445	
				≈ 140	*570*	*400 ± 100*
623				*≈ 200*	*300*	*150 ± 50*

[a] Dipole remains stable

anism. These velocity-length measurements at 523 K and 140 MPa can be used to evaluate the attempt frequency ν of the mobility law. Fitting Eq. 11 to experimental data, we obtain $\nu \approx 1.2\ 10^{15}$ Hz (this value will be discussed in detail later), leading to a very good agreement between the theoretical and experimental velocities (see the red symbols and the red full line in Fig. 10). For this applied stress and this temperature, the mobility model predicts a critical kink-pair extension $L_{kp}^* = 800$ nm. Dislocations with a length L_d greater than this critical length should have a constant velocity, as predicted by the kink-collision regime. We could not observe long-enough dislocations to confirm this saturation of the dislocation velocity. Nevertheless, the experimental observation of a macro-jog on a screw dislocation of 600 nm length (Figs. 9(e) and 9(f)) indicates that the critical kink-pair extension should be slightly larger than 600 nm, thus corroborating the theoretical value. One can also notice that the experimental measurements for the two largest dislocation lengths, around 550 nm, lead to velocities slightly lower than predicted by the linear relation, in agreement with a progressive transition between the length-dependent and the kink collision regimes at around 600 nm.

Two other velocity-length measurements corresponding to shorter dislocations in thinner zones of the microsample were obtained at 523 K. They are plotted in Fig. 10, using blue and green symbols. For both data-sets, the velocity varies linearly with the dislocation length, without reaching the saturation corresponding to the kink-collision regime. It has not been possible to determine experimentally the applied stress in the same regions of the sample corresponding to these measurements. We use instead the now fully parameterized mobility law to find the stresses that best fit both velocity-length data-sets. We obtain τ_a = 194 MPa and 245 MPa for the blue and green sets respectively. The increase of the applied stress is consistent with the decreasing sample thickness. These values are in the same range as the values of the stress measured in other regions of the thin foil and reported in Table 2, thus illustrating the reliability of the analytical model to describe dislocation velocity. For these two applied stresses, the mobility law predicts a critical kink-pair extension $L_k{}^*_p$ slightly larger than the lengths of the dislocations which could be observed in TEM experiments, still in agreement with the length-dependent regime seen in the experiments.

4.2.2. Experiments at 573 K

The values of the line tension stress $\tau_l(d)$ measured for expanding dipoles at 573 K in the thickest parts of microsamples (> 400 nm) are almost equal to those measured at 523 K in the same conditions (Table 2). Unfortunately, we have no estimate of the friction stress τ_f at this temperature, and thus the applied stress τ_a cannot be estimated unambiguously. Nevertheless, since τ_f should be slightly lower at 573 K than at 523 K on account of the thermally activated diffusion of solutes, we

cation length to enforce a null velocity when the dislocation length tends to zero. The same 50 nm shift is applied to other data appearing in Fig. 10 and corresponding to different applied stresses.

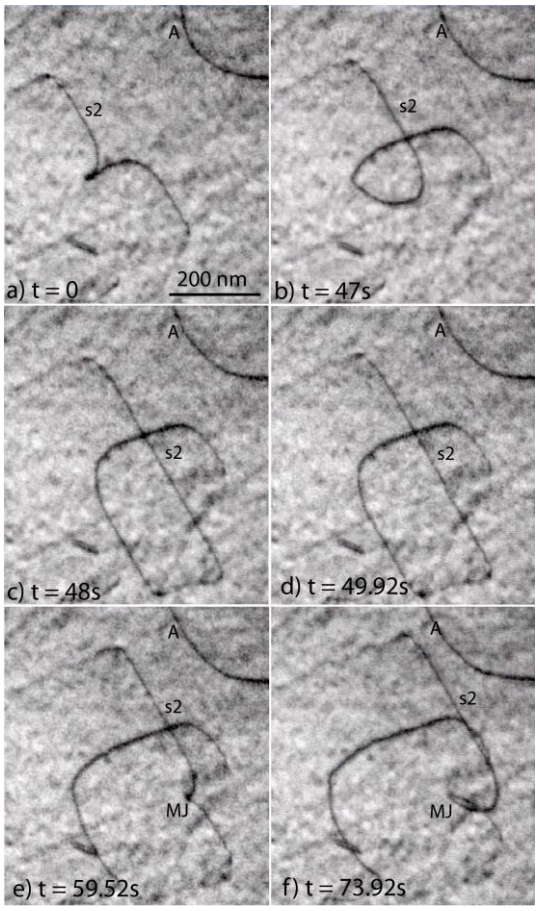

Figure 9: Glide motion of a screw dislocation s2 of variable length at 523 K (same zone as in Fig. 8). See corresponding video as Supplementary material.

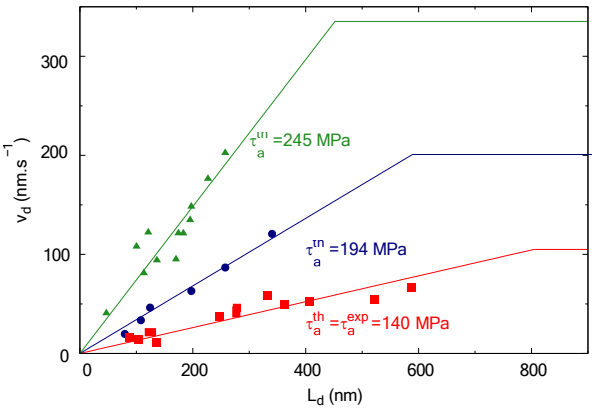

Figure 10: Experimental and theoretical screw dislocation velocities as a function of their lengths at 523 K. The symbols correspond to three sets of measurements in three different regions with different applied stresses τ_a^{exp}, the solid lines to the theoretical velocity for the applied stress τ_a^{th} (Eq. 11) (linear part: length-dependent regime, saturated part: kink-collision regime). The lower experimental data in red are obtained from dislocation s2 in Fig. 9.

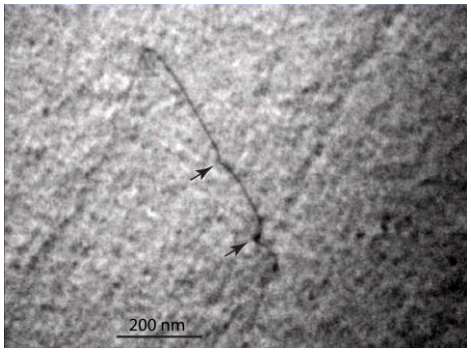

Figure 11: Moving screw dislocation with two macro-jogs indicated by arrows at 573 K. See corresponding video as Supplementary material.

can assume that τ_a is also only slightly lower, say between 130 MPa and 140 $\pm$ 25 MPa. We do not have any precise measurement of the dislocation velocity as a function of length at 573 K.

At this temperature and applied stress, the theoretical value of the kink-pair critical extension is in the range between 370 and 500 nm. Fig. 11 shows a screw dislocation of true length 760 nm anchored at two macro-jogs formed by a cross-kink mechanism. Other dislocations of true length 400 nm to 750 nm exhibit single similar macro-jog cusps. This indicates that the critical extension of a kink-pair $L_k{}^*{}_p$ is probably close to 400 nm at 573 K for a stress of 130–140 MPa, thus in agreement with the theoretical value.

4.2.3. *Experiments at 623 K*

We have neither stress measurement at this temperature, nor any determination of dislocation velocity as a function of length. However, the shear stress in the thinner parts of the order of 300 nm should be lower than 270 MPa, the stress measured in such a similar thin part at 523 K (see Table 2), namely of the order of 200 $\pm$30 MPa. This will lead to a kink-pair critical extension between 160 and 200 nm. Fig. 12 shows dislocation structures similar to those schematised in Fig. 7(c), in a zone of 300 nm thickness. These dislocations are curved with a short segment in pure screw orientation of average length 150 nm, which indicates that $L_k{}^*{}_p$ is close to 150$\pm$50 nm for a stress of the order of 200 MPa, thus fully compatible with the theoretical value.

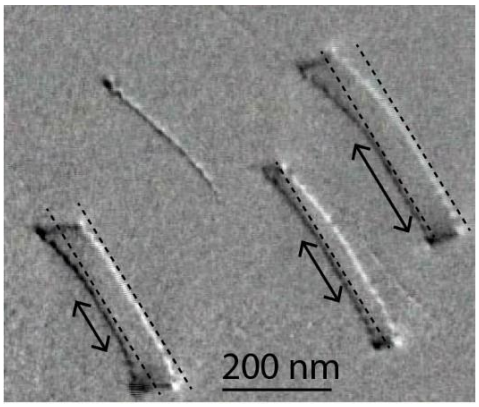

Figure 12: Difference images showing the glide motion of curved screw dislocations at 623 K. The motion takes place to the right and the two images are separated by 0.48 s. The dislocations are pure screw (locally parallel to the dotted lines) over the arrowed length, as schematised in Fig. 7(c).

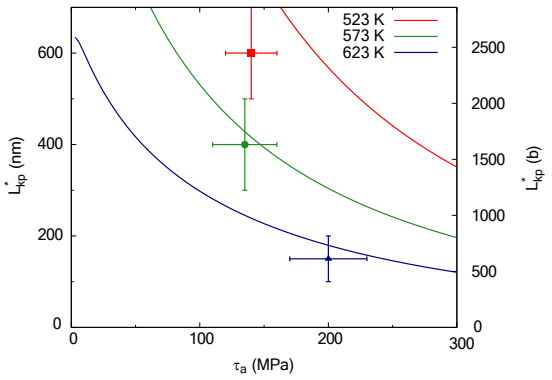

Figure 13: Experimental (symbols) and theoretical values (full lines) of the mean free path of kink-pairs $L_k{}^*{}_p$ as a function of applied stress for three different temperatures.

4.2.4. *Kink-pair critical extension*

All stress measurements and corresponding estimates of the kink-pair mean free path $L_k{}^*{}_p$ are summarized in Table 2. In Fig. 13, we plot the predicted L^*_{kp} as a function of applied stress at 523, 573 and 623 K, and compare them to the theoretical values given by Eq. 12 for the three same temperatures using DFT data only. $L_k{}^*{}_p$ depends strongly on the applied stress at the three temperatures. Experimental estimates fall very close to the model predictions at 573 and 623 K. At 523 K, the gap between the measurements and the model predictions is more pronounced. At this temperature and 140 MPa, the theoretical value of the kink-pair critical extension is 800 nm, which is larger than the experimental value of 600 $\pm$ 100 nm. But the difference remains acceptable given the simplifications used in the model and the uncertainties in the experimental measurements, which are based on a very few observations, as discussed in the next section. Meanwhile, the experimental value $L_k{}^*{}_p$ = 600 $\pm$ 100 nm corresponds to applied stresses in the range 190 MPa to 270 MPa, which is consistent with the experimental value of 140 MPa given its uncertainties.

4.3. *Discussion*

This detailed comparison between the mobility law parameterized on ab initio calculations and experimental measurements obtained from in-situ TEM straining experiments show the ability of the kinetic model to describe dislocation velocity in this temperature range where C atoms segregate in the core of screw dislocations. A similar conclusion was reached in bcc tungsten in presence of carbon [31], but the more detailed experimental data obtained here in iron allow us to show that this modeling approach is also quantitative.

In view of the uncertainties associated with the experimental determination of the kink-pair critical extension L^*_{kp}, and also of the applied stress, experimental values of L^*_{kp} agree reasonably well with the theoretical values deduced from the analytical mobility law. Eq. (12) shows that this critical extension $L_k{}^*{}_p$ does not depend on migration energies of kinks and mainly depends on their formation energy. This good agreement gives confidence in the value of the kink-pair formation energy obtained from ab initio calculations. A less satisfying agreement is obtained for the lowest temperature, 523 K. This temperature corresponds to the beginning of the reappearance of the Peierls regime observed experimentally [1, 2]. It is therefore possible that C diffusion is still not fast enough at this temperature to lead to a full decoration of the reconstructed dislocation core with one carbon atom every other prismatic site, as predicted by thermodynamics [17]. It is also possible that other interstitial sites around the reconstructed dislocation core trap some C atoms, despite their lower segregation energy [9, 17].

Previous in-situ straining experiments [1, 2] have shown that the end of dynamic strain ageing (DSA) in iron corresponds to the temperature where screw dislocations decorated by C atoms recover their mobility. Caillard and Bonneville [1, 2] thus concluded that the activation energy experimentally known at the end of DSA, between 1.3 and 1.7 eV, should correspond to the activation energy of the Peierls mechanism controlling glide of screw dislocations at these high temperatures. This perfectly agrees with our ab initio calculations. In

the length-dependent regime, the activation energy entering in the expression of the dislocation velocity (Eq. 11) is $2E_f^{\infty} + E_{mig} = 1.74$ eV, whereas in the kink-collision regime it is $E_f^{\infty} + E_{mig} = 1.32$ eV, considering that $E_{mig} = \min(E_{mig}^{K^+}, E_{mig}^{K^-})$. The values given by ab initio calculations for both the kink-pair formation and the kink migration energies appear therefore relevant when compared to experiments.

We note that the fitted frequency $\nu^- = 1.2 \times 10^{15}$ Hz is much larger than the Debye frequency ν_D generally taken for the attempt frequency in the literature ($\nu_D \approx 10^{13}$ Hz in Fe). The contribution from entropy terms to the total free activation energy can be invoked to explain this discrepancy. A similar effect was recently reported in molecular dynamics simulations of dislocation-carbon interactions in Fe [16]. Replacing $2E_f^{\infty}$ by the free energy, $2E_f^{\infty} - TS_f$ and taking the attempt frequency equal to the Debye frequency, we find that 5 k_B would be needed for the entropy contribution to the kink-pair formation.

5. Conclusions

An ab initio-informed mobility law for dislocation glide in Fe-C proceeding through the formation and propagation of kink-pairs is proposed in the temperature range where carbon segregates on screw dislocations, based on a quantitative comparison with experimental measurements. TEM in-situ straining experiments performed in Fe-C in the high-temperature regime allow to measure the dislocation velocities at different temperatures and local shear stresses, as well as to estimate the value of the critical kink-pair extension marking the transition between the length-dependent and kink-collision regimes. These experimental measurements are very delicate and require to take all necessary precautions. Meanwhile modelling at the atomic scale a kink-pair on a screw dislocation decorated with one carbon atom every other prismatic site (as predicted by ab initio based-thermodynamics [17] in the high-temperature regime) allows to compute its formation, migration and nucleation energies using ab initio calculations. The resulting analytical dislocation velocity, fully parameterized on the DFT values obtained for kink energies, is compared with the experimental measurements. A general good agreement is obtained between the experimental and theoretical velocities given the uncertainties in the experimental measurements. The present combined experimental and numerical study provides an indirect confirmation that carbon atoms can reconstruct the core of screw dislocations in bcc metals. It also shows that DFT can reliably predict the formation and migration energies of kinks on carbon-decorated dislocations. The mobility law determined here can be used in higher-scale models and in particular in dislocation dynamics simulations to study the plasticity in FeC alloys at elevated temperatures.

Acknowledgments

The authors acknowledge support from the ANR through the DeGAS project (ANR-16-CE08-0008). The authors also acknowledge support from the GENCI-TGCC and GENCI-IDRIS computer centers under grant No. A0070906821 and from PRACE for funding DIMAB project by providing computing time on the Juwels supercomputer at Jülich Supercomputing Centre. This work has been carried out within the framework of the EUROfusion Consortium, funded by the European Union via the Euratom Research and Training Program (Grant Agreement No 101052200–EUROfusion). Views and opinions expressed are however those of the author(s) only and do not necessarily reflect those of the European Union or the European Commission. Neither the European Union nor the European Commission can be held responsible for them.

Appendix A. Elastic interaction energy between kinks

The total elastic correction, W_{int}^{tot}, can be expressed in terms of the interaction energy between two opposite kinks $W_{int}(w_{kp}) = \frac{1}{2}(E(0) + E^{pj}(0))$:

$$W_{int}^{tot} = \frac{1}{2}\sum_{n=-\infty}^{+\infty} W_{int}(w_{kp} + nh) - \frac{1}{2}\sum_{n=-\infty,\, n\neq 0}^{+\infty} W_{int}(nh) + \frac{1}{2}\sum_{n=-\infty}^{+\infty} W_{int}(-w_{kp} + nh) - \frac{1}{2}\sum_{n=-\infty,\, n\neq 0}^{+\infty} W_{int}(nh), \quad \text{(A.1)}$$

where h is the cell size along the dislocation line, i.e. the distance along b between kinks of the same sign. The first (resp. third) term on the right-hand side of Eq. A.1 corresponds to the interaction between the positive (resp. negative) kink in the cell and all the negative (resp. positive) kinks (the one contained in the cell and its periodic images). The second (resp. fourth) term refers to the interaction between the positive (resp. negative) kink in the cell and all the other positive (resp. negative) kinks. The factor 1/2 comes from the fact that half of this interaction energy is devoted to each kink of

the different pairs. By rearranging the total interaction energy as the sum of the kink-pair interaction with its periodic images ($W^{\mathrm{PBC}}_{\mathrm{int}}$) and of the interaction between the opposite kinks in the simulation cell ($W^{\mathrm{supercell}}_{\mathrm{int}}$), we obtain:

$$W^{\mathrm{PBC}}_{\mathrm{int}} = -\frac{E(0) + E^{\mathrm{JJ}}(0)}{2}\lambda_{\mathrm{p}}^2 + \sum_{n=1}^{\infty}\left(\frac{1}{|w_{\mathrm{kp}} + nh|} + \frac{1}{|-w_{\mathrm{kp}} + nh|} - \frac{2}{|nh|}\right), \tag{A.2}$$

$$W^{\mathrm{supercell}}_{\mathrm{int}} = W_{\mathrm{int}}(w_{\mathrm{kp}}). \tag{A.3}$$

In the case of $w_{\mathrm{kp}} = h/2$, the series converges towards Eq. 2.

References

[1] D. Caillard, J. Bonneville, Dynamic strain aging caused by a new Peierls mechanism at high-temperature in iron, Scripta Mater. 95 (2015) 15–18. doi:doi:10.1016/j.scriptamat.2014.09.019.

[2] D. Caillard, Dynamic strain ageing in iron alloys: The shielding effect of carbon, Acta Mater. 112 (2016) 273–284. doi:doi:10.1016/j.actamat.2016.04.018.

[3] G. C. Soares, R. R. U. Queiroz, L. A. Santos, Effects of dynamic strain aging on strain hardening behavior, dislocation substructure, and fracture morphology in a ferritic stainless steel, Metall. Mater. Trans. A 51 (2020) 725–739. doi:doi:10.1007/s11661-019-05574-6.

[4] D. Caillard, Kinetics of dislocations in pure Fe. Part I. In situ straining experiments at room temperature, Acta Mater. 58 (2010) 3493–3503. doi:doi:10.1016/j.actamat.2010.02.023.

[5] L. Ventelon, B. Lüthi, E. Clouet, L. Proville, B. Legrand, D. Rodney, F. Willaime, Dislocation core reconstruction induced by carbon segregation in BCC iron, Phys. Rev. B 91 (2015) 1–5. doi:doi:10.1103/PhysRevB.91.220102.

[6] S. S. Sarangi, A. K. Kanjarla, An atomistic study of the influence of carbon on the core structure of screw dislocation in bcc Fe and its consequences on non-schmid behavior, Mater. Today Commun. 31 (2022) 103285. doi:doi:10.1016/j.mtcomm.2022.103285.

[7] Z.-Q. Wang, Y.-H. Li, G.-H. Lu, H.-B. Zhou, Influence of carbon and oxygen on the core structure and Peierls stress of screw dislocation in molybdenum, Metals 12 (2022). doi:doi:10.3390/met12030507.

[8] A. Bakaev, A. Zinovev, D. Terentyev, G. Bonny, C. Yin, N. Castin, Y. A. Mastrikov, E. E. Zhurkin, Interaction of carbon with microstructural defects in a W-Re matrix: An ab initio assessment, J. Appl. Phys. 126 (2019) 075110–17. doi:doi:10.1063/1.5094441.

[9] B. Lüthi, L. Ventelon, C. Elsässer, D. Rodney, F. Willaime, First principles investigation of carbon-screw dislocation interactions in body-centered cubic metals, Modelling Simul. Mater. Sci. Eng. 25 (2017) 084001. doi:doi:10.1088/1361-651X/aa88eb.

[10] G. Hachet, L. Ventelon, F. Willaime, E. Clouet, Screw dislocation-carbon interaction in bcc tungsten: an ab initio study, Acta Mater. 200 (2020) 481–489. doi:doi:10.1016/j.actamat.2020.09.014.

[11] Y. Zhao, L. Dezerald, J. Marian, Electronic structure calculations of oxygen atom transport energetics in the presence of screw dislocations in tungsten, Metals 9 (2019) 252. doi:doi:10.3390/met9020252.

[12] B. Lüthi, L. Ventelon, D. Rodney, F. Willaime, Attractive interaction between interstitial solutes and screw dislocations in BCC iron from first principles, Comput. Mater. Sci. 148 (2018) 21–26. doi:doi:10.1016/j.commatsci.2018.02.016.

[13] P. P. P. O. Borges, E. Clouet, L. Ventelon, Ab initio investigation of the screw dislocation-hydrogen interaction in bcc tungsten and iron, Acta Mater. 234 (2022) 118048. doi:doi:10.1016/j.actamat.2022.118048.

[14] Y.-H. Li, H.-B. Zhou, F. Gao, G. Lu, G.-H. Lu, F. Liu, Hydrogen induced dislocation core reconstruction in bcc tungsten, Acta Mater. 226 (2022) 117622. doi:doi:10.1016/j.actamat.2022.117622.

[15] P. Grigorev, T. D. Swinburne, J. R. Kermode, Hybrid quantum/classical study of hydrogen-decorated screw dislocations in tungsten: Ultrafast pipe diffusion, core reconstruction, and effects on glide mechanism, Phys. Rev. Mater. 4 (2020) 023601. doi:doi:10.1103/PhysRevMaterials.4.023601.

[16] A. Allera, F. Ribeiro, M. Perez, D. Rodney, Carbon-induced strengthening of bcc iron at the atomic scale, Phys. Rev. Mater. (2022) 013608. doi:doi:10.1103/PhysRevMaterials.6.013608.

[17] B. Lüthi, F. Berthier, L. Ventelon, B. Legrand, D. Rodney, F. Willaime, Ab initio thermodynamics of carbon segregation on dislocation cores in bcc iron, Modelling Simul. Mater. Sci. Eng. 27 (2019) 074002. doi:doi:10.1088/1361-651X/ab28d4.

[18] D. Rodney, L. Ventelon, E. Clouet, L. Pizzagalli, F. Willaime, Ab initio modeling of dislocation core properties in metals and semiconductors, Acta Mater. 124 (2017) 633–659. doi:doi:10.1016/j.actamat.2016.09.049.

[19] L. Ventelon, F. Willaime, E. Clouet, D. Rodney, Ab initio investigation of the Peierls potential of screw dislocations in bcc Fe and W, Acta Mater. 61 (2013) 3973–3985. doi:doi:10.1016/j.actamat.2013.03.012.

[20] G. Kresse, J. Furthmüller, Efficient iterative schemes for *ab initio* total-energy calculations using a plane-wave basis set, Phys. Rev. B 54 (1996) 11169–11186. doi:doi:10.1103/PhysRevB.54.11169.

[21] P. E. Blöchl, Projector augmented-wave method, Phys. Rev. B 50 (1994) 17953–17979. doi:doi:10.1103/PhysRevB.50.17953.

[22] G. Kresse, D. Joubert, From ultrasoft pseudopotentials to the projector augmented-wave method, Phys. Rev. B 59 (1999) 1758–1775. doi:doi:10.1103/PhysRevB.59.1758.

[23] T. D. Swinburne, S. L. Dudarev, S. P. Fitzgerald, M. R. Gilbert, A. P. Sutton, Theory and simulation of the diffusion of kinks on dislocations in bcc metals, Phys. Rev. B 87 (2013) 064108. doi:doi:10.1103/PhysRevB.87.064108.

[24] S. Chiesa, P. M. Derlet, S. L. Dudarev, H. V. Swygenhoven, Optimization of the magnetic potential for α-Fe, J. Phys. Condens. Matter 23 (2011) 206001. doi:doi:10.1088/0953-8984/23/20/206001.

[25] M. Mrovec, D. Nguyen-Manh, C. Elsässer, P. Gumbsch, Magnetic bond-order potential for iron, Phys. Rev. Lett. 106 (2011) 246402. doi:doi:10.1103/PhysRevLett.106.246402.

[26] J. Chaussidon, M. Fivel, D. Rodney, The glide of screw dislocations in bcc Fe: Atomistic static and dynamic simulations, Acta Mater. 54 (2006) 3407–3416. doi:doi:j.actamat.2006.03.044.

[27] L. Ventelon, F. Willaime, P. Leyronnas, Atomistic simulation of single kinks of screw dislocations in α-Fe, J. Nucl. Mater. 386–388 (2009) 26–29. doi:doi:10.1016/j.jnucmat.2008.12.053.

[28] A. Seeger, C. Wüthrich, Dislocation relaxation processes in body-centred cubic metals, Il Nuovo Cimento 33 (1976) 38–75. doi:doi:10.1007/BF02722472.

[29] L. Dezerald, L. Proville, L. Ventelon, F. Willaime, D. Rodney, First-principles prediction of kink-pair activation enthalpy on screw dislocations in BCC transition metals: V, Nb, Ta, Mo, W, and Fe, Phys. Rev. B 91 (2015) 1–7. doi:doi:10.1103/PhysRevB.91.094105.

[30] A. Ghafarollahi, W. A. Curtin, Theory of double-kink nucleation in dilute bcc alloys, Acta Mater. (2020) 635–650. doi:doi:https://doi.org/10.1016/j.actamat.2020.07.008.

[31] G. Hachet, D. Caillard, L. Ventelon, E. Clouet, Mobility of screw dislocation in BCC tungsten at high temperature in presence of carbon, Acta Mater. 222 (2022) 117440. doi:doi:10.1016/j.actamat.2021.117440.

[32] J. Lothe, Dislocations in continuous elastic media, in: V. L. Indenbom, J. Lothe (Eds.), Elastic strain fields and dislocation mobility, volume 31, Elsevier, North-Holland, Amsterdam, 1992, pp. 201–203. doi:doi:10.1016/B978-0-444-88773-3.50008-X.

[33] E. Clouet, Babel software, 2007. URL: http://emmanuel.clouet.free.fr/Programs/Babel/index.html.

[34] B. Lüthi, Modelisation *ab initio* des interactions entre dislocations vis et solutes interstitiels dans les metaux de transition cubiques centres, Ph.D. thesis, Univ. Lyon, France, 2017.

[35] C. Becquart, J. Raulot, G. Bencteux, C. Domain, M. Perez, S. Garruchet, H. Nguyen, Atomistic modeling of an Fe system with a small concentration of C, Comput. Mater. Sci. 40 (2007) 119–129. doi:doi:10.1016/j.commatsci.2006.11.005.

[36] D. E. Jiang, E. A. Carter, Carbon dissolution and diffusion in ferrite and austenite from first principles, Phys. Rev. B 67 (2003) 214103–11. doi:doi:10.1103/PhysRevB.67.214103.

[37] J. R. G. da Silva, R. B. McLellan, Diffusion of carbon and nitrogen in B.C.C. iron, Mater. Sci. Eng. 26 (1976) 83. doi:doi:10.1016/0025-5416(76)90229-9.

[38] J. P. Hirth, J. Lothe, Theory of dislocations, second ed., Wiley, New York, 1982.

[39] D. Caillard, J. L. Martin, Thermally Activated Mechanisms in Crystal Plasticity, Pergamon Materials Series, Pergamon Press, 2003.

[40] G. Po, Y. Cui, D. Rivera, D. Cereceda, T. D. Swinburne, J. Marian, N. Ghoniem, A phenomenological dislocation mobility law for bcc metals, Acta Mater. 119 (2016) 123–135. doi:doi:10.1016/j.actamat.2016.08.016.

[41] D. Caillard, Kinetics of dislocations in pure Fe. Part II. In situ straining experiments at low temperature, Acta Mater. 58 (2010) 3504–3515. doi:doi:10.1016/j.actamat.2010.02.024.

[42] D. Caillard, A TEM in situ study of the softening of tungsten by rhenium, Acta Mater. 194 (2020) 249–256. doi:doi:10.1016/j.actamat.2020.04.039.

Figure 1(a)

Click here to access/download;Figure(s);visu_vesta_4b_C-C1b.eps

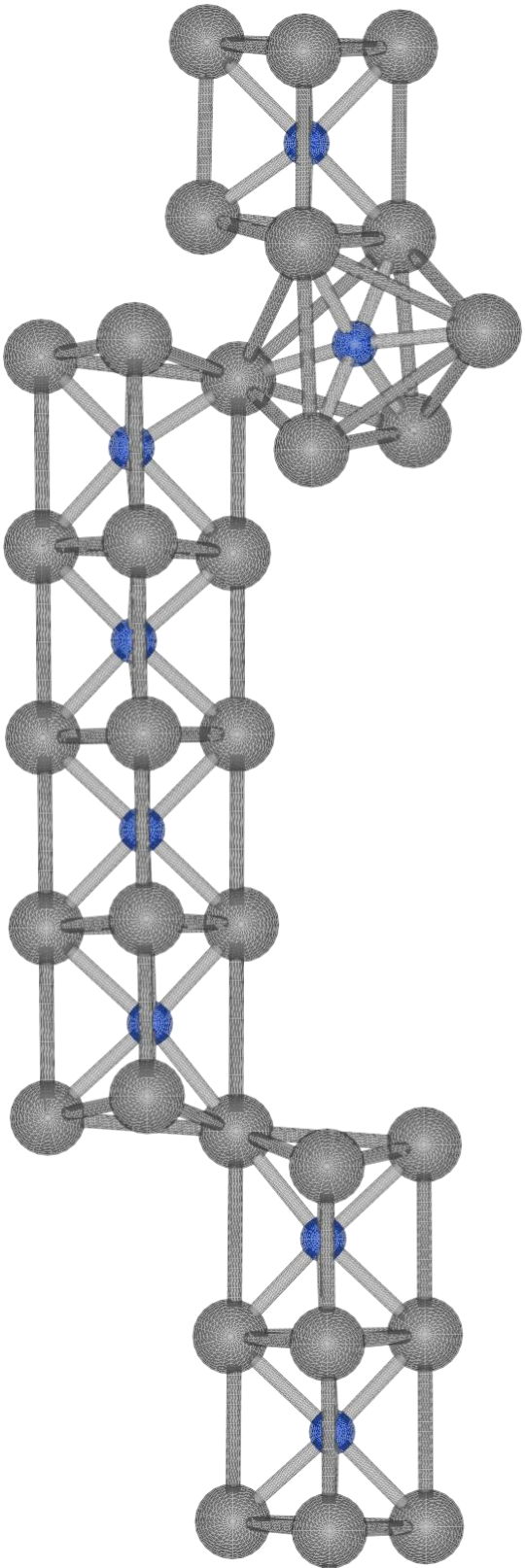

Figure 1(b)

Click here to access/download;Figure(s);visu_vesta_4b_C-C2b.eps

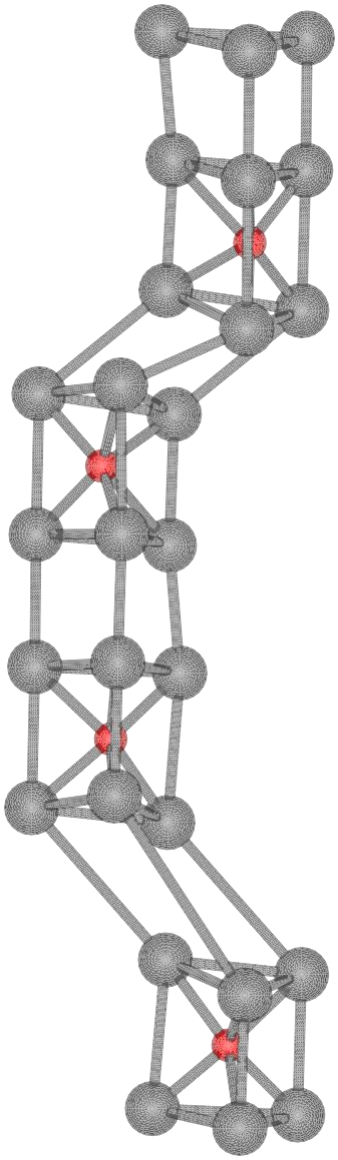

Figure 1(c)

Click here to access/download;Figure(s);kink_schema2_2b.eps

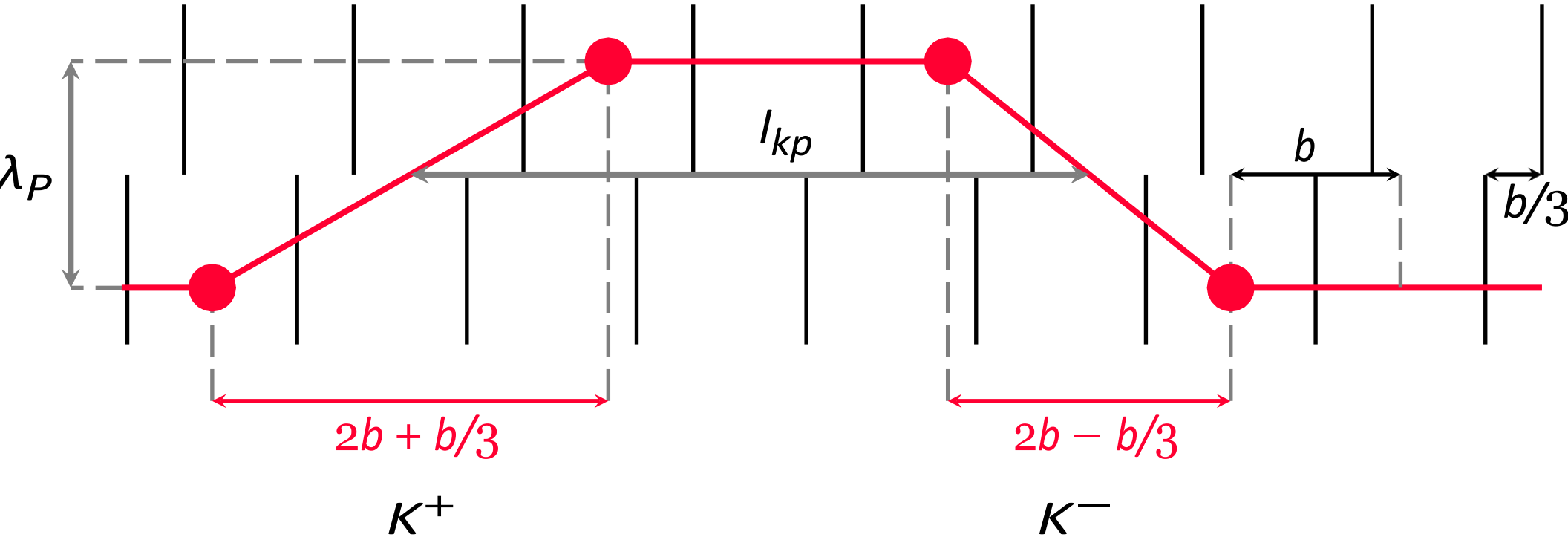

Figure 2(a)

Click here to access/download;Figure(s);ef_dft_corrected_1b.eps

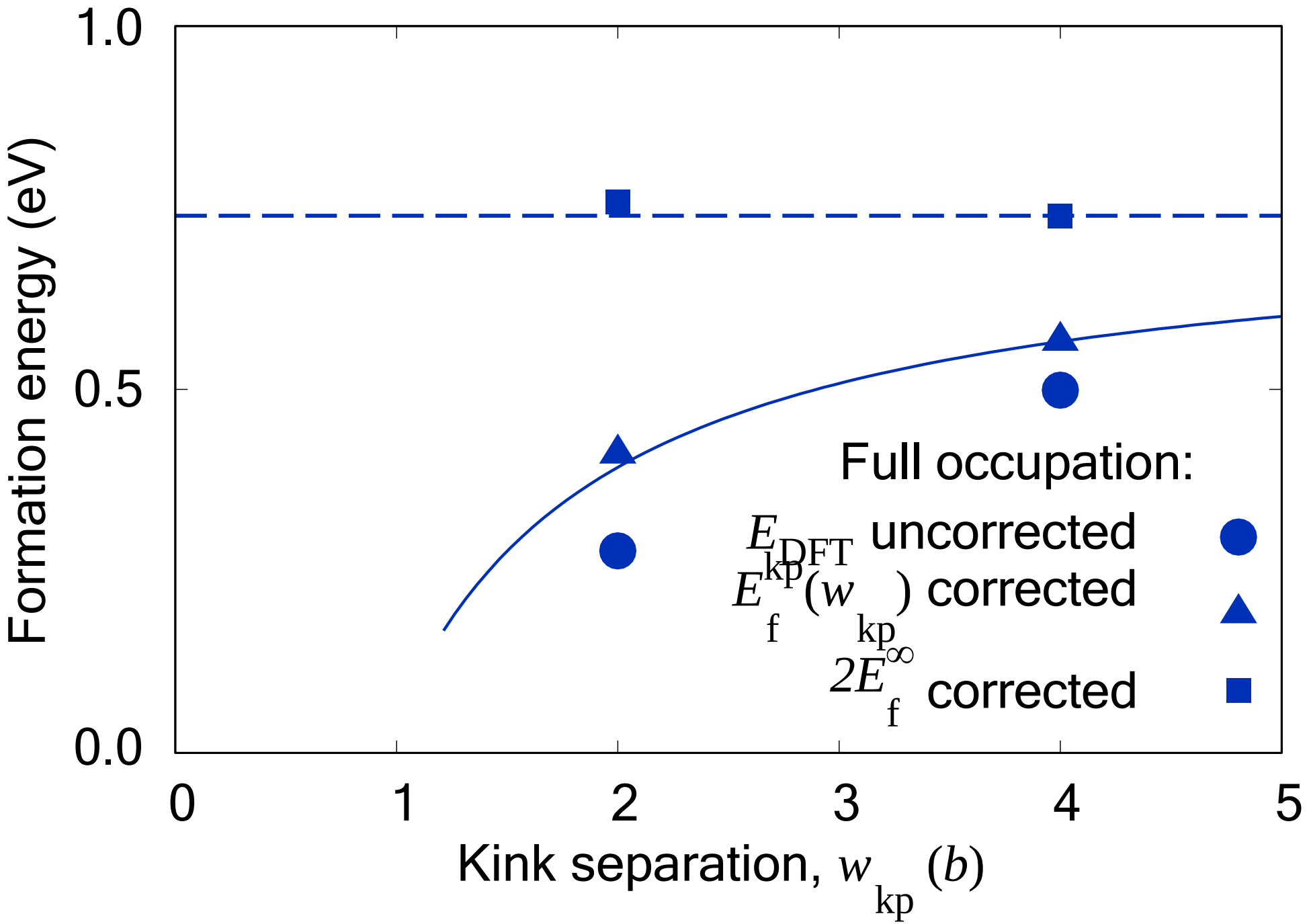

Figure 2(b)

Click here to access/download;Figure(s);ef_dft_corrected_2b.eps

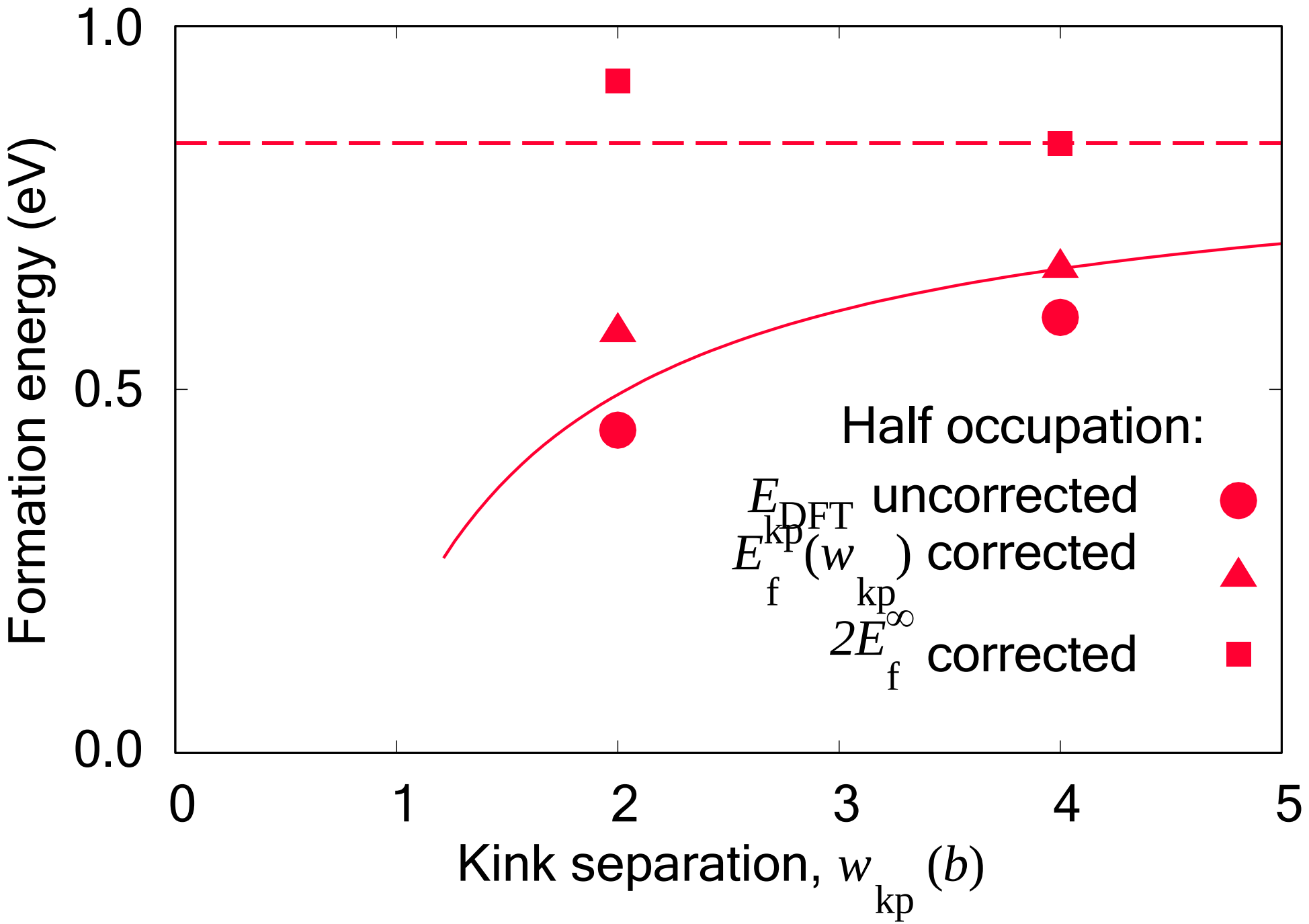

Figure 3(a)

Click here to access/download;Figure(s);migration_k+_v2-figure0.eps

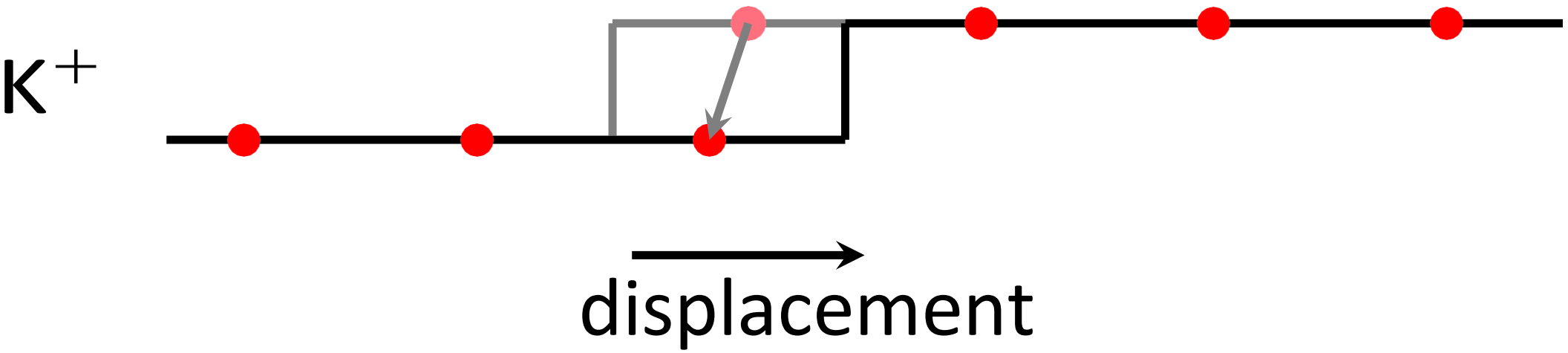

Figure 3(b)

Click here to access/download;Figure(s);migration_k-_v2-figure0.eps

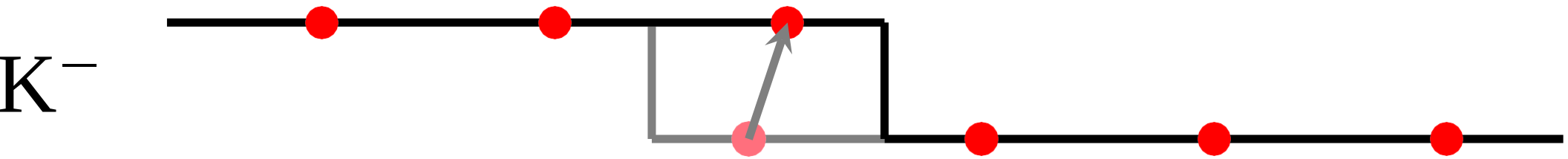

Figure 3(c)

Click here to access/download;Figure(s);mep.eps

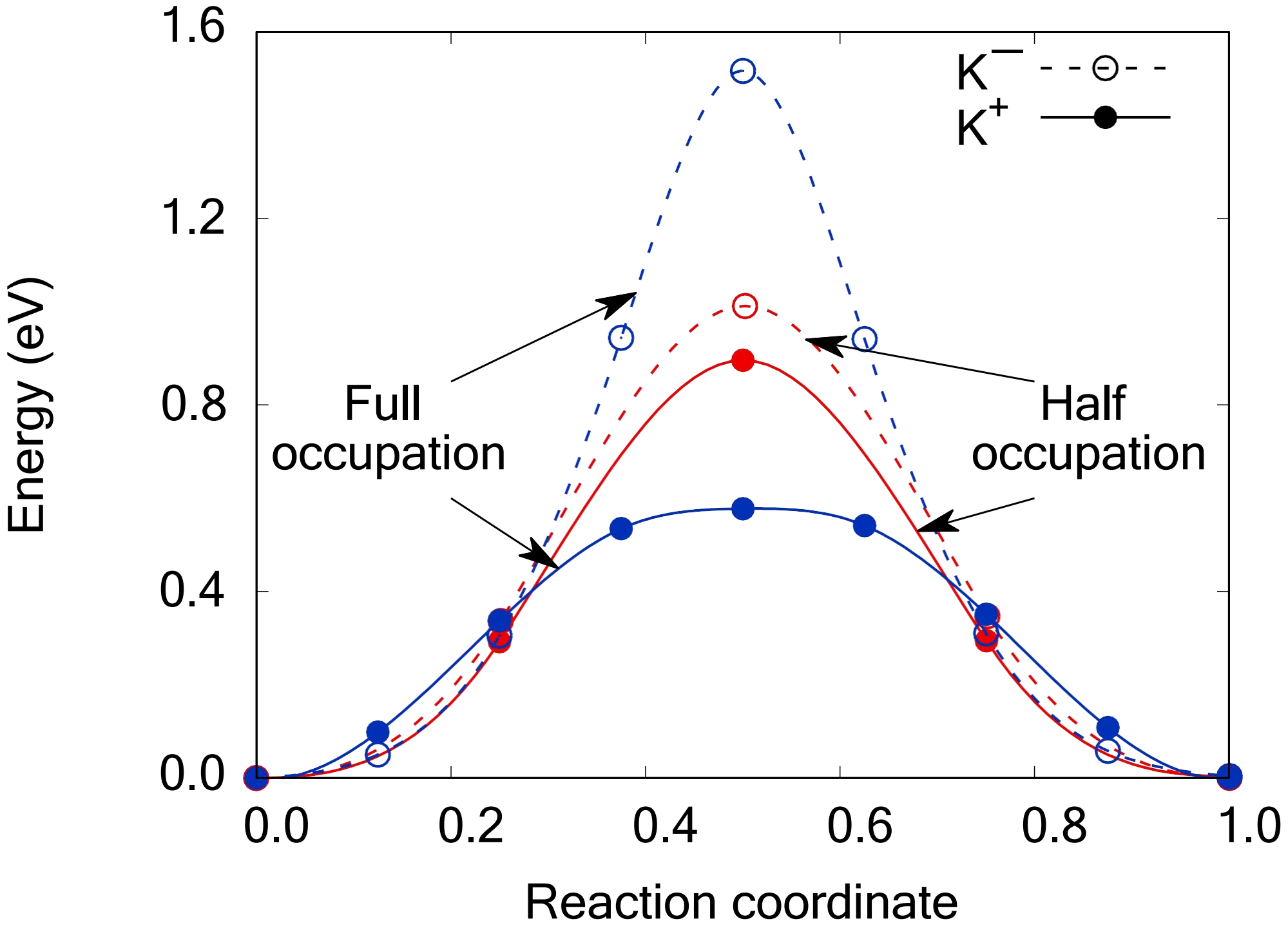

Figure 4

Click here to access/download;Figure(s);mep_nucleation.eps

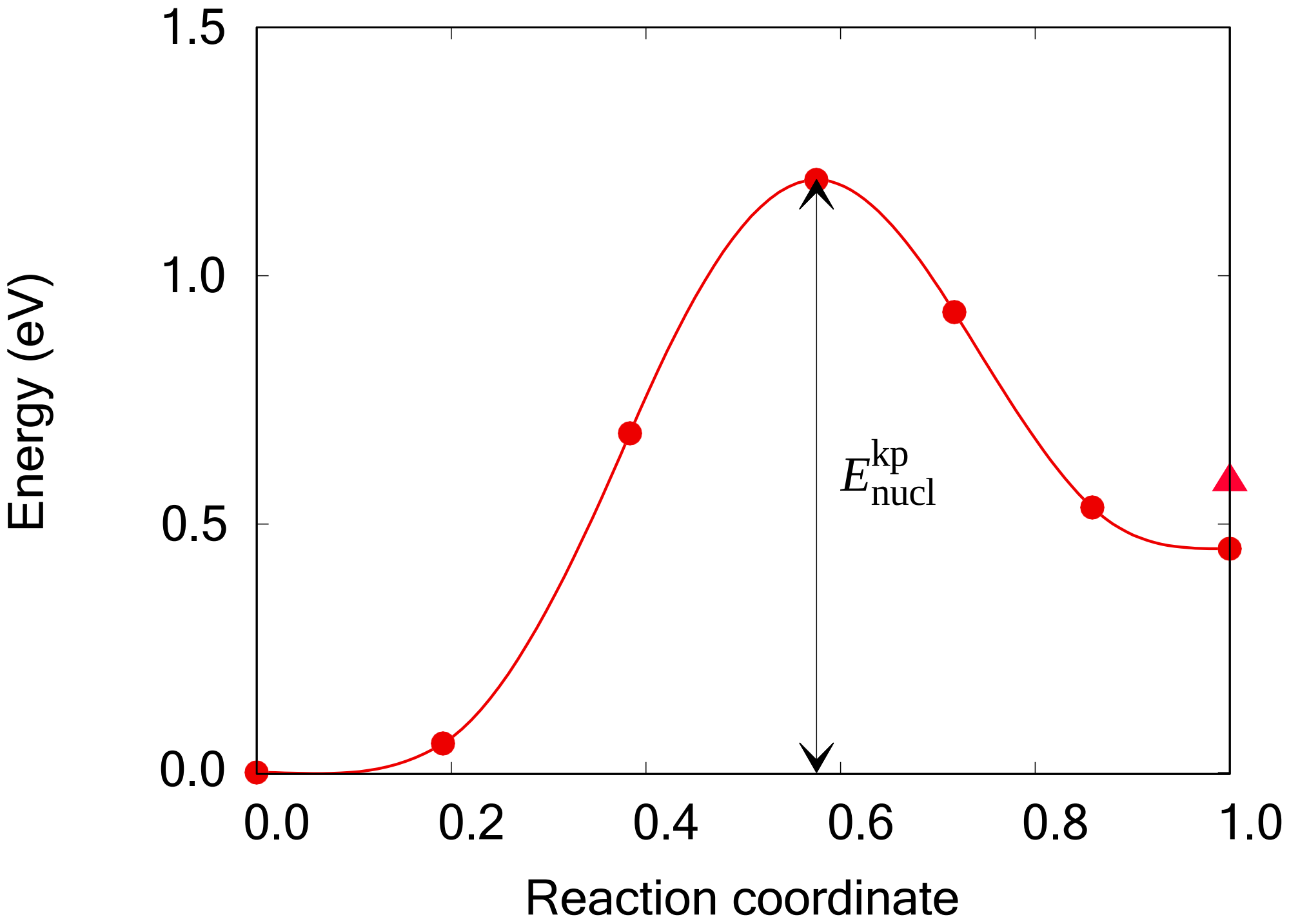

Figure 4

Click here to access/download;Figure(s);ei-figure0.eps

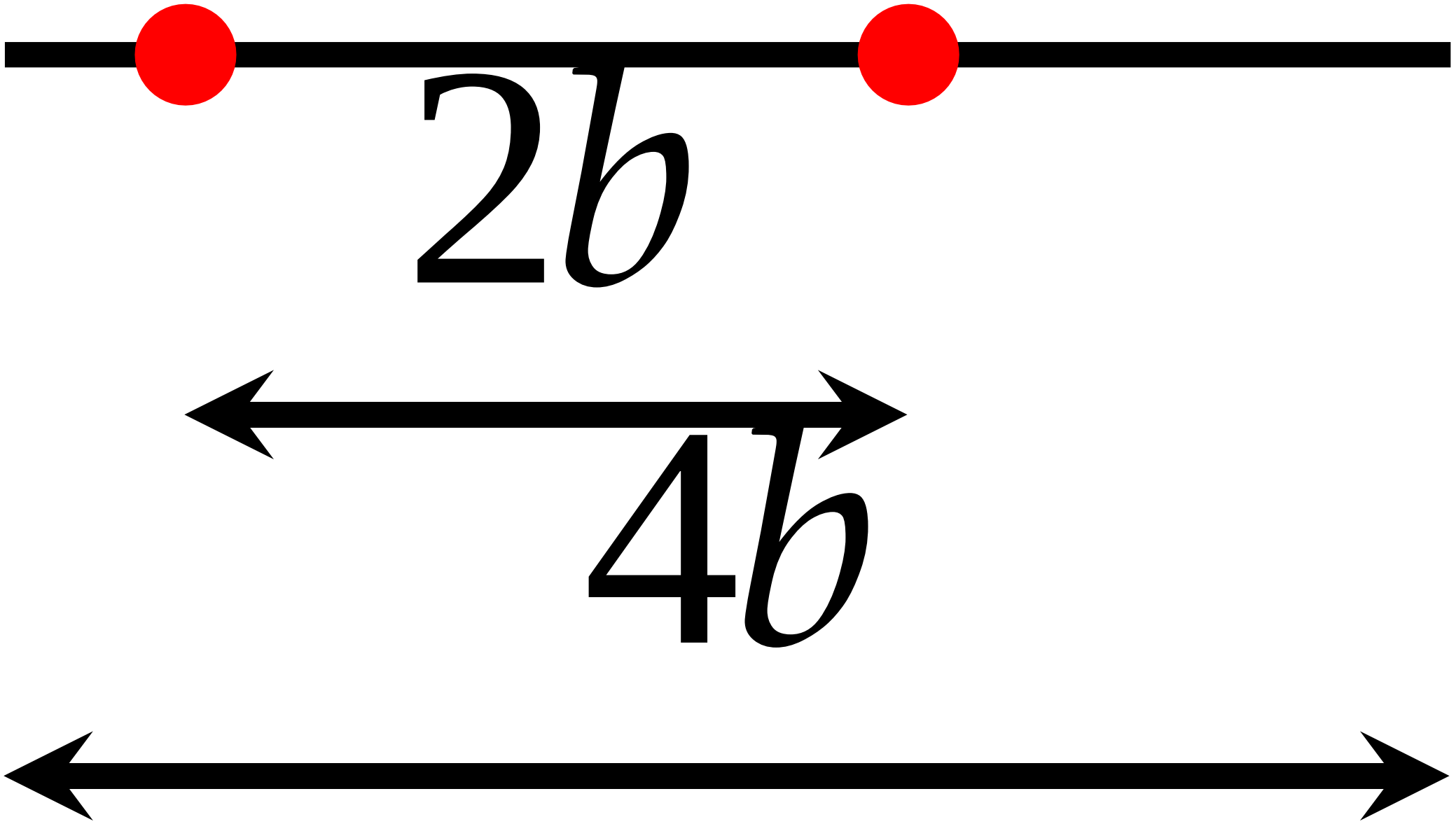

Figure 4

Click here to access/download;Figure(s);ef-figure0.eps

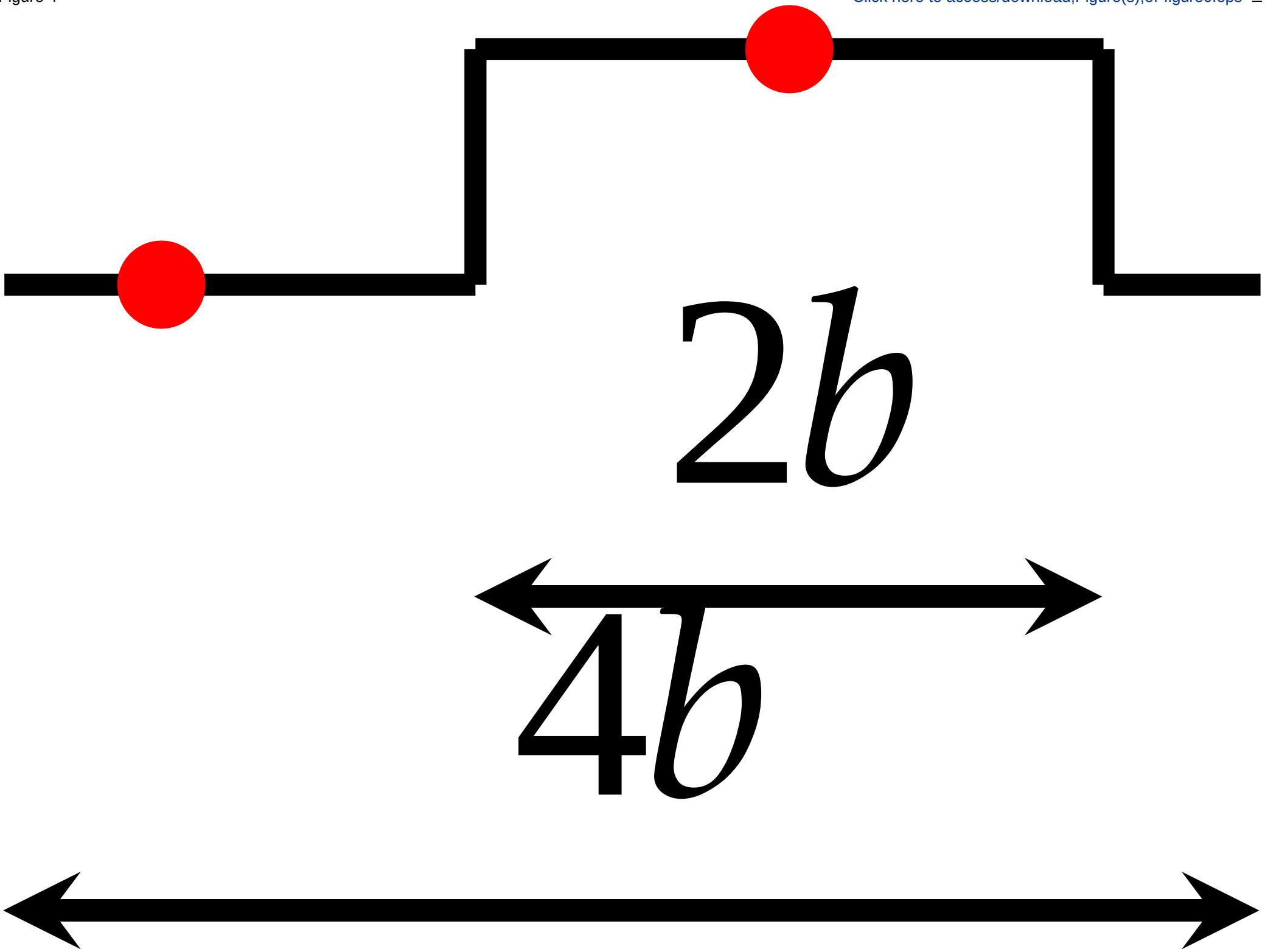

Figure 5

Click here to access/download;Figure(s);kink-pair_model.eps

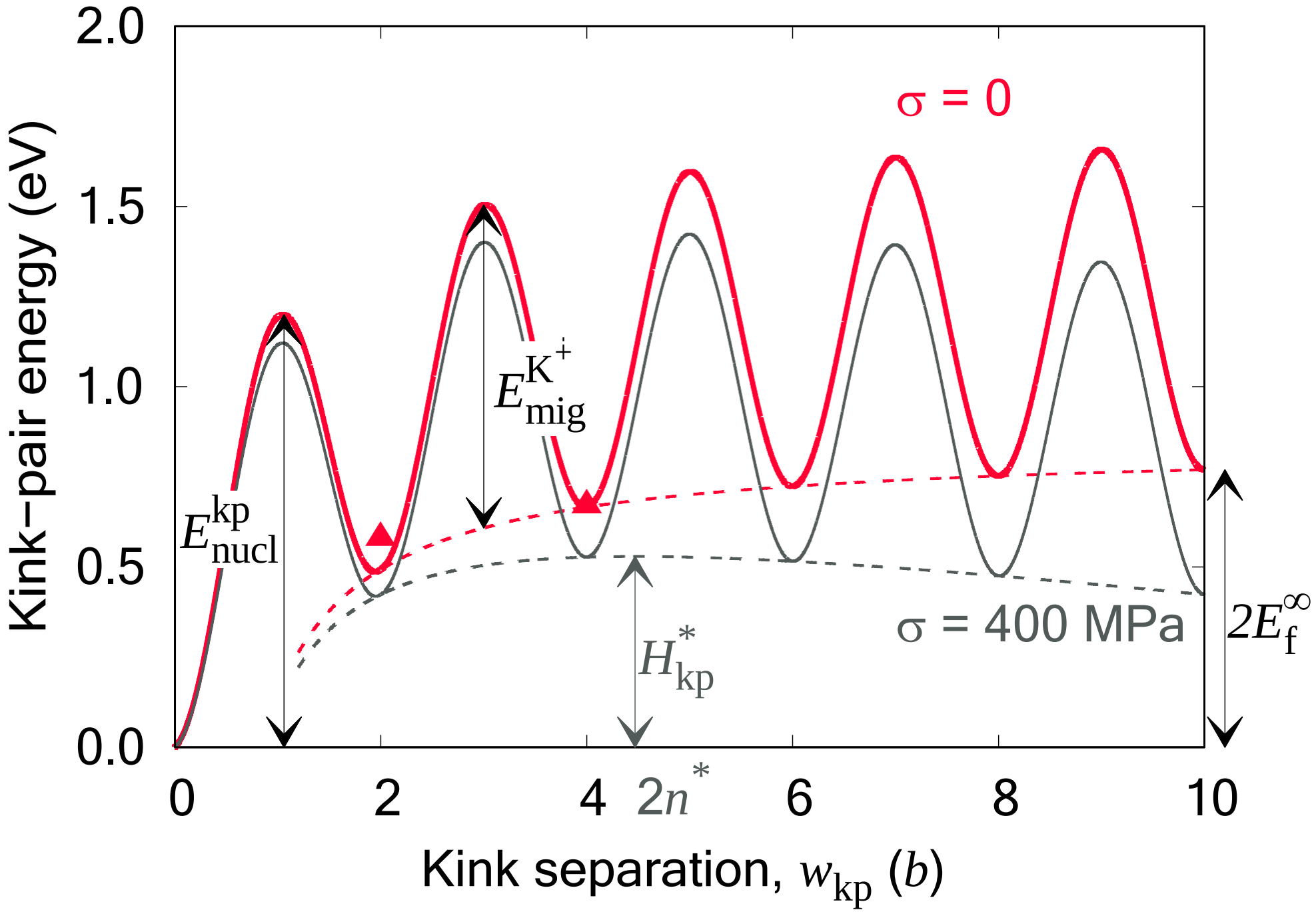

Click here to access/download;Figure(s);exp_fig1.jpg

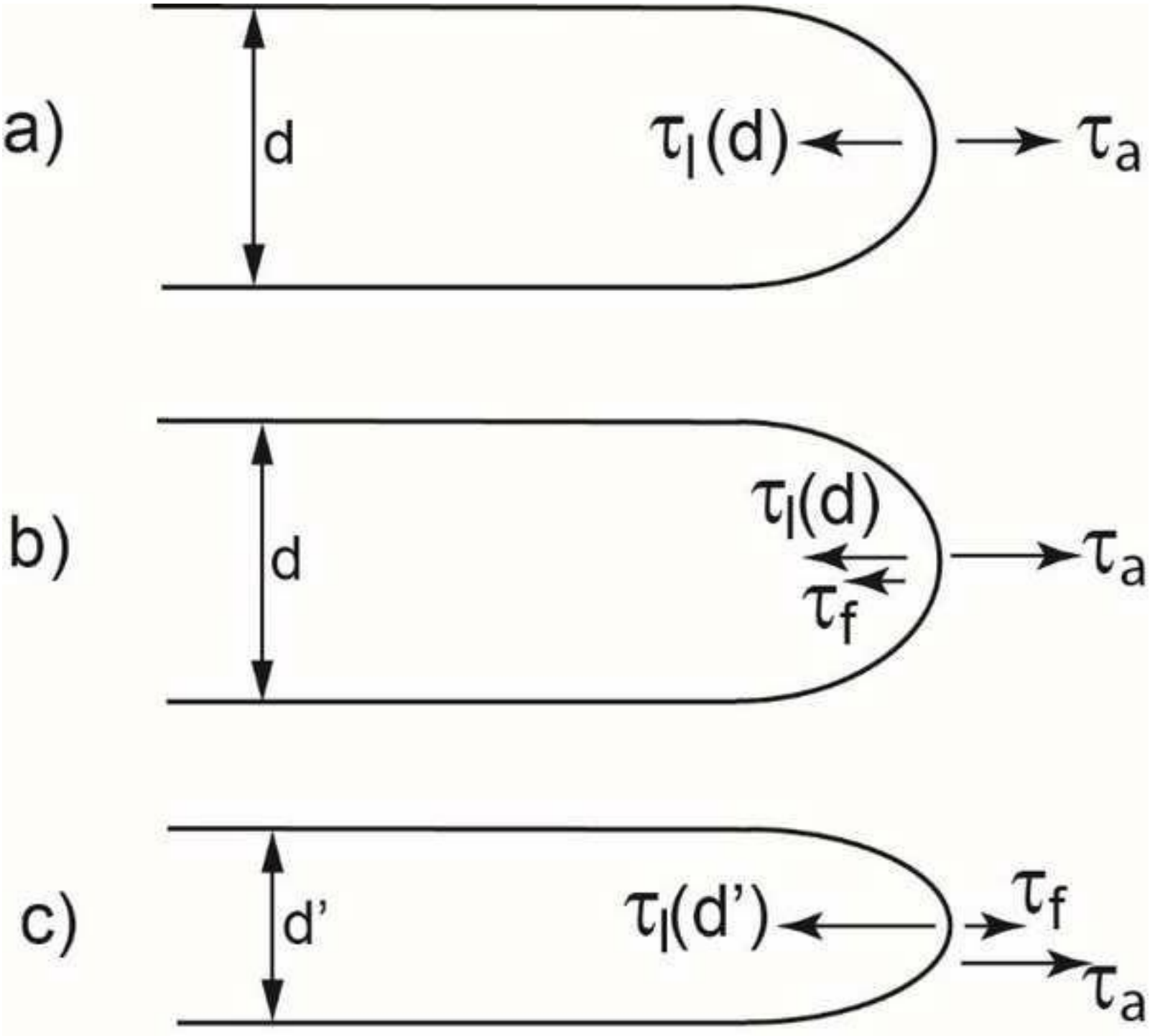

Figure 7

Click here to access/download;Figure(s);exp_fig2.pdf

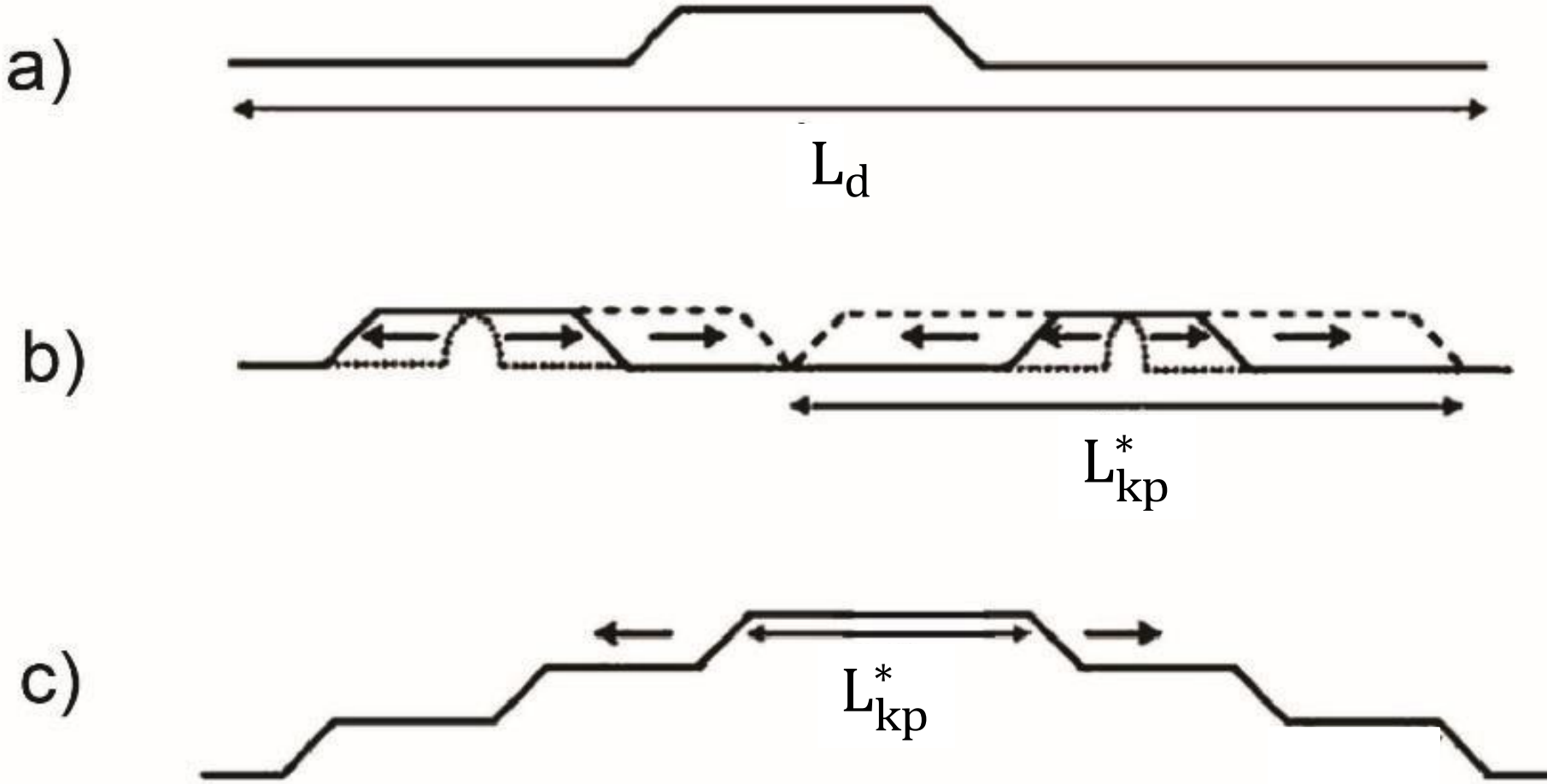

Figure 8

Click here to access/download;Figure(s);exp_fig3.jpg

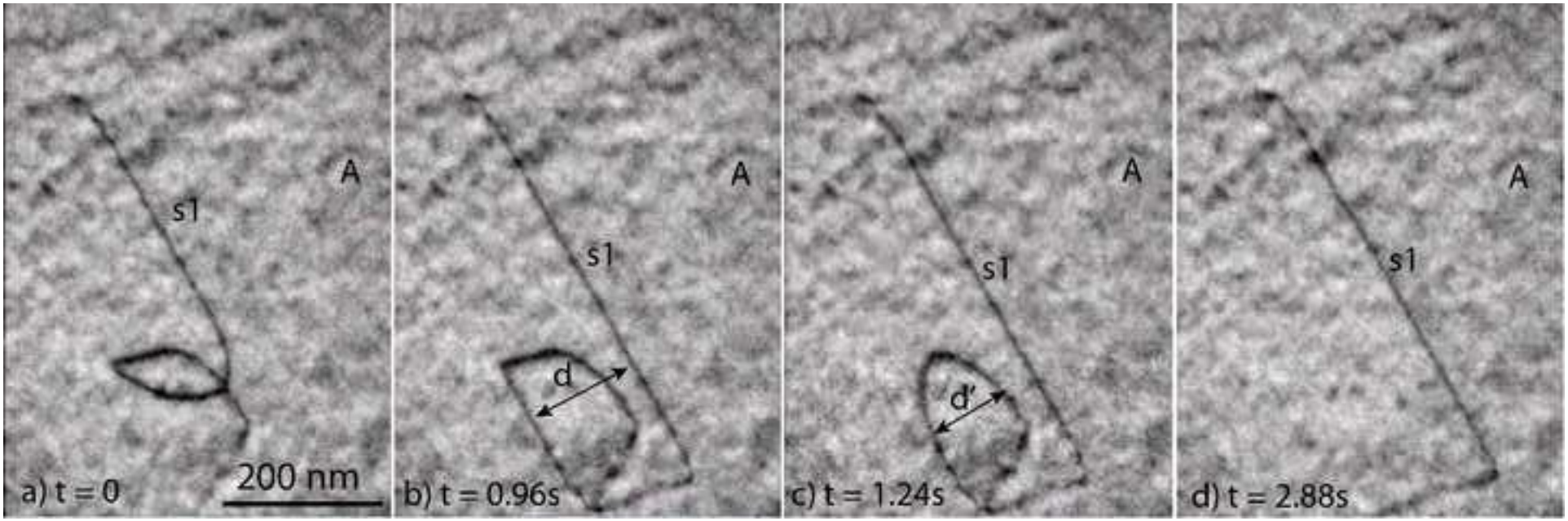

Figure 9

Click here to access/download;Figure(s);exp_fig4_new.jpg

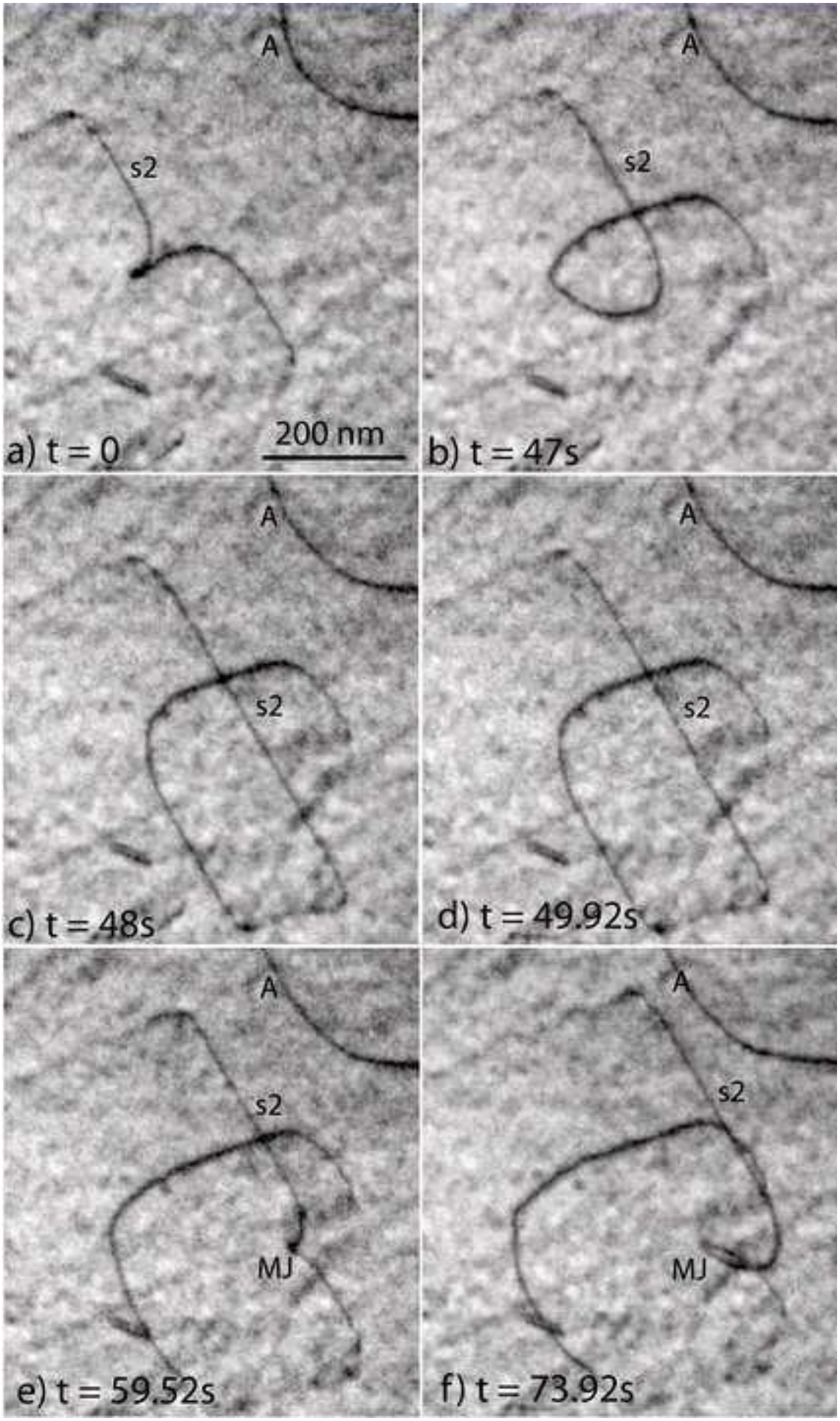

Figure 10

Click here to access/download;Figure(s);exp_fig5.eps

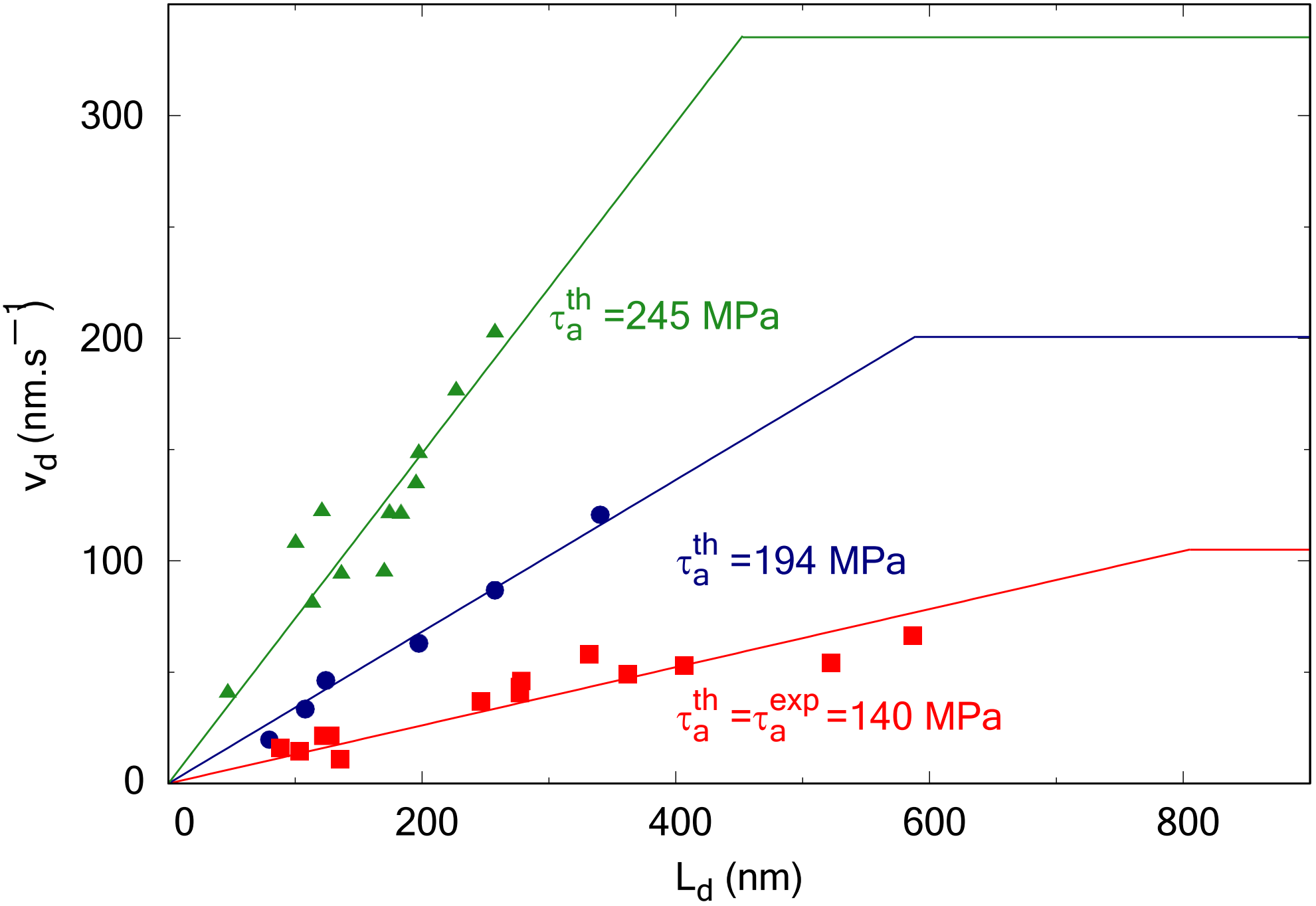

Figure 11

Click here to access/download;Figure(s);exp_fig6_new.jpg

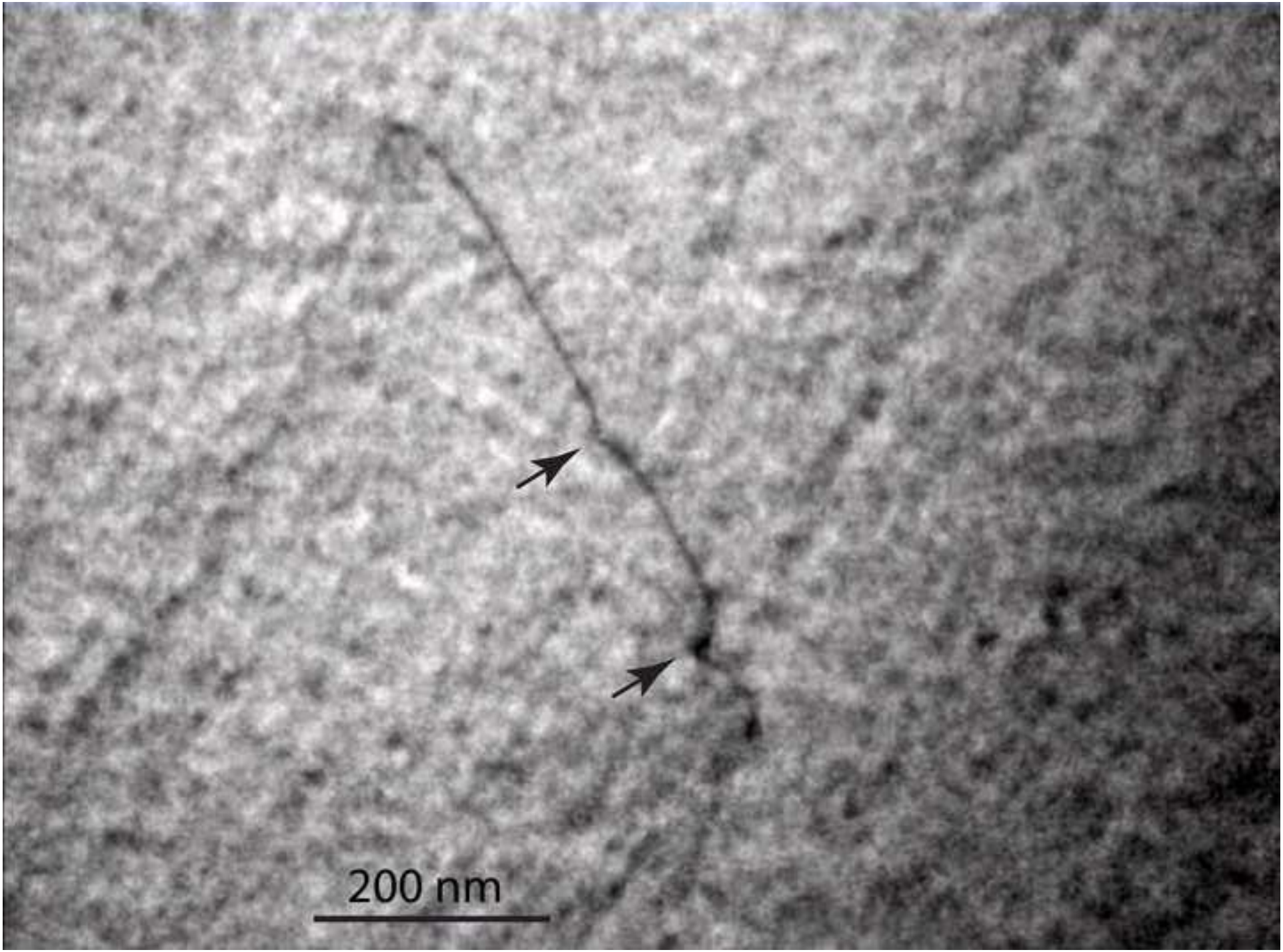

Figure 12

Click here to access/download;Figure(s);exp_fig7.jpg

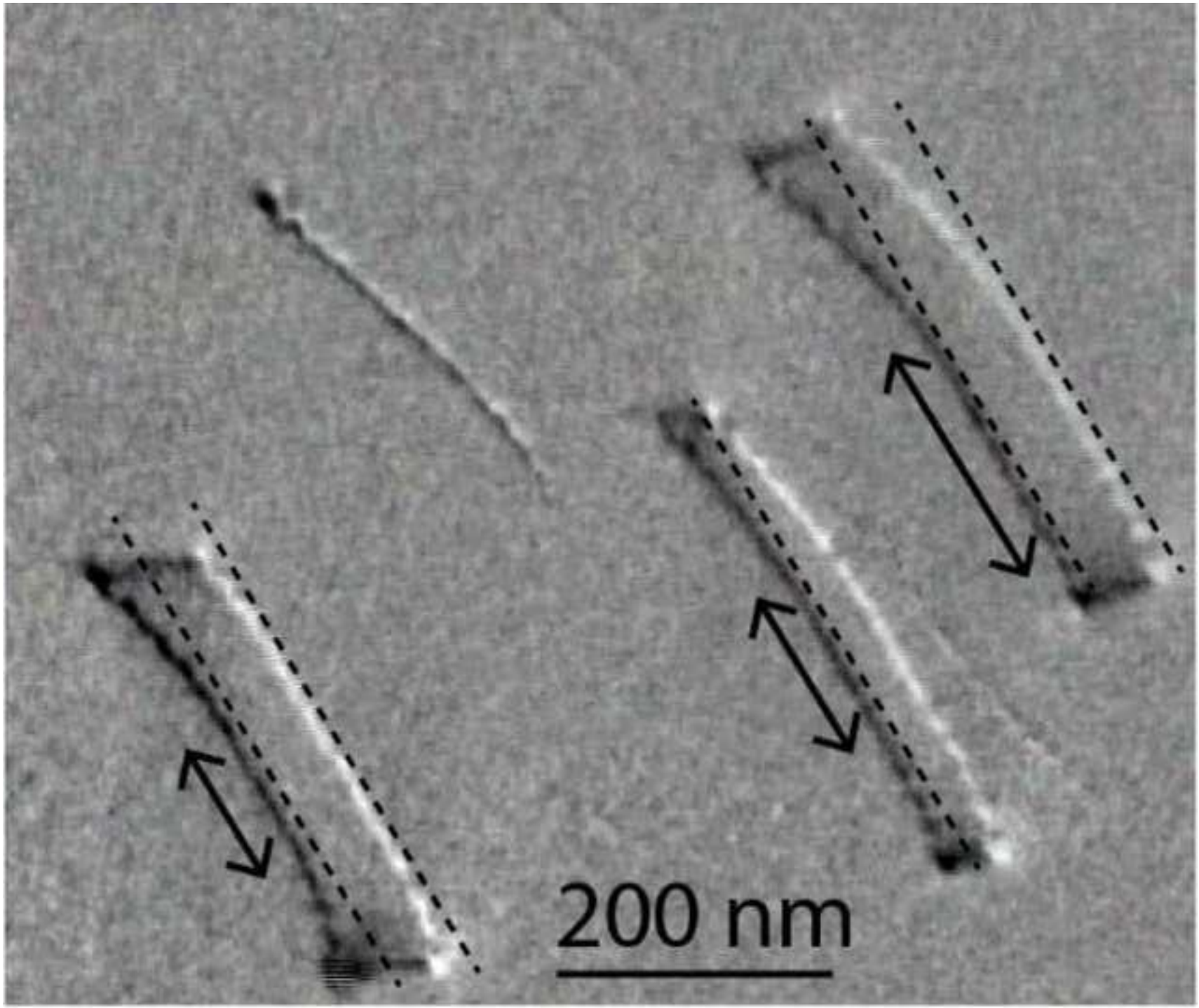

Figure 13

Click here to access/download;Figure(s);exp_fig8.eps

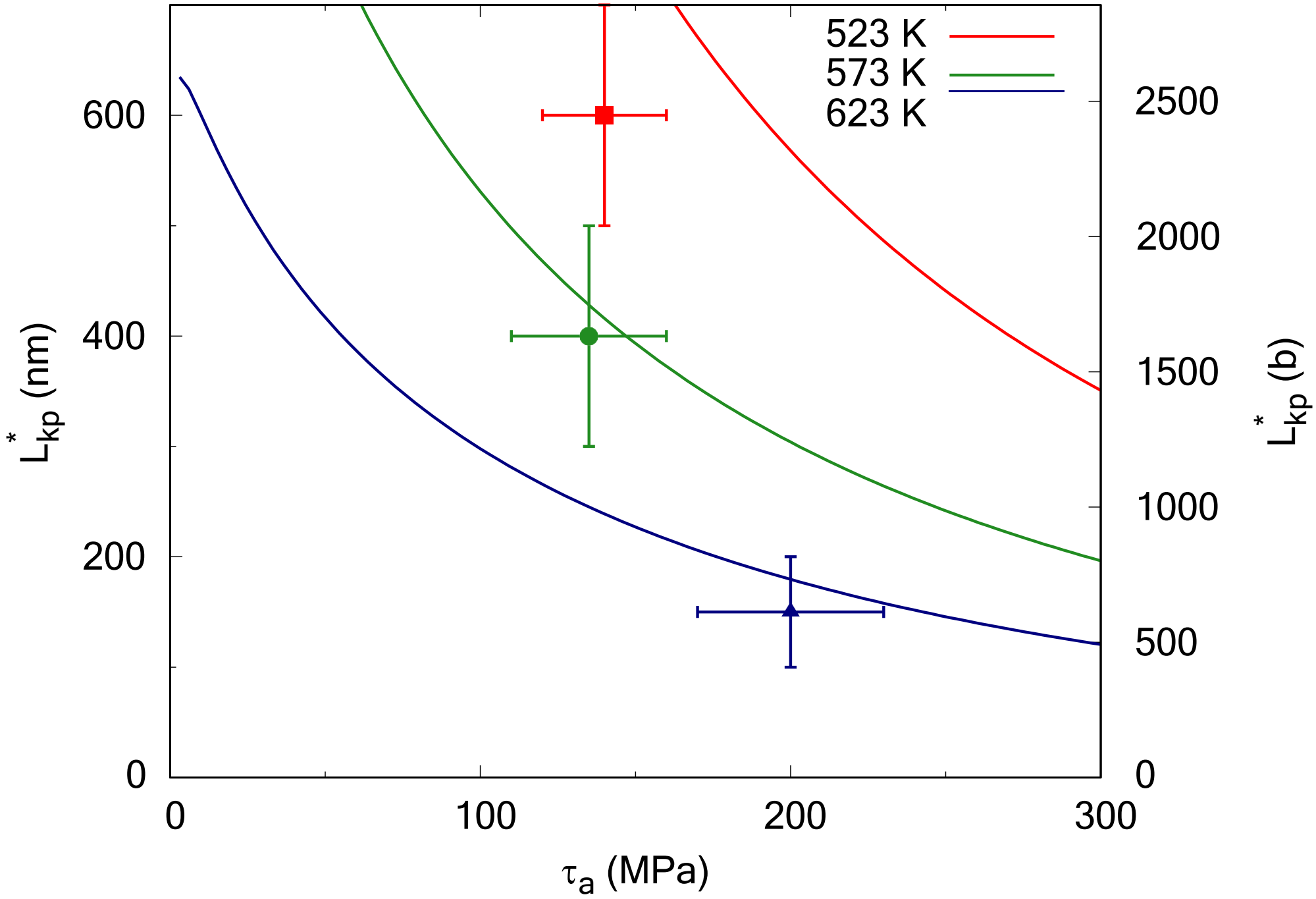

Video of figure 8 (slowed down by a factor of 5)

Click here to access/download
Supplementary Material
video-fig.8(div.5).avi

Video of figure 11 (slowed down by a factor of 5)

Click here to access/download
Supplementary Material
video-fig.11(div.5).avi

Video of figure 9

Click here to access/download
Supplementary Material
video-fig.9.avi

Graphical Abstract

Ab initio calculations + NEB

Formation and migration of kink-pairs

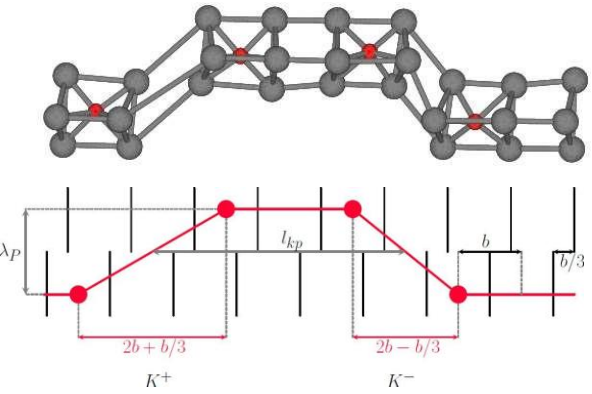

Dislocation mobility law

Analytical model (CNT)

→ **Dislocation velocity:** $v_d(\tau_a, T, b)$

In-situ TEM straining experiments

Fe + 16 appm C

523 K < T < 623 K

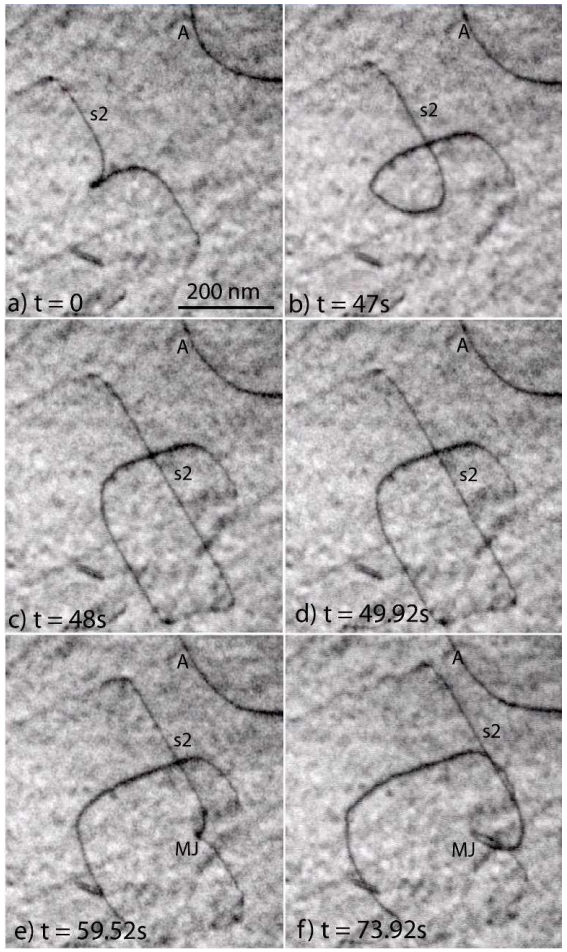

Experiment/theory comparison

Dislocation velocity, local stress and kink-pair critical extension

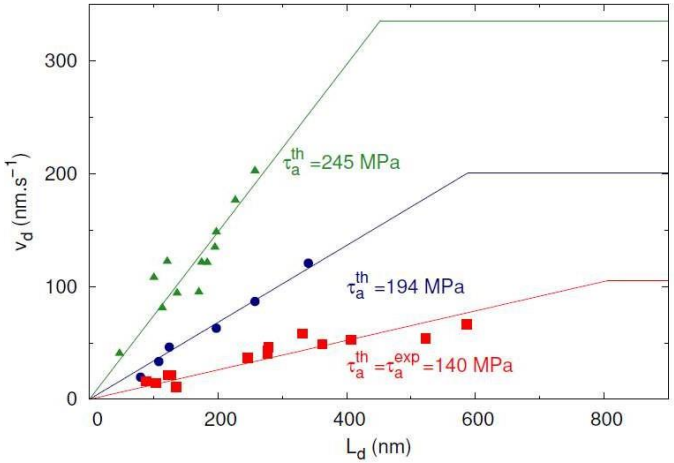

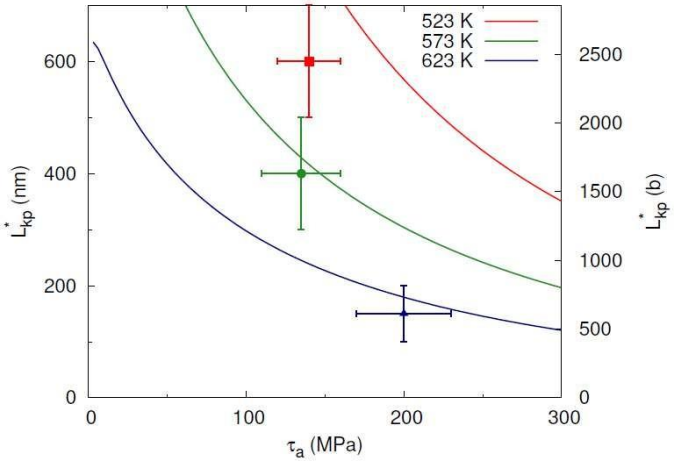

Declaration of Interest Statement